Clays and Clay Minerals, Vol. 64, No. 2, 86–107, 2016.

THERMAL CONSTRAINTS ON CLAY GROWTH IN FAULT GOUGE AND THEIR RELATIONSHIP WITH FAULT-ZONE EVOLUTION AND HYDROTHERMAL ALTERATION: CASE STUDY OF GOUGES IN THE KOJAKU GRANITE, CENTRAL JAPAN

Masakazu Niwa[1,*], Koji Shimada[2], Hajimu Tamura[1], Kenji Shibata[1], Shigeru Sueoka[2], Ken-ichi Yasue[1], Tsuneari Ishimaru[2], and Koji Umeda[1]

[1] Toki Research Institute of Isotope Geology and Geochronology, Japan Atomic Energy Agency, Toki, Gifu, 509-5102, Japan
[2] Monju Project Management and Engineering Center, Japan Atomic Energy Agency, Tsuruga, Fukui, 919-1279, Japan

Abstract—In order to elucidate the process of mineralization of clay minerals in fault gouge and its spatial-temporal relationship with fault-zone evolution and hydrothermal alteration, X-ray diffraction (XRD) analysis and K-Ar dating were performed on clay samples from the Kojaku Granite of central Japan, including fault gouge along an active fault. The area studied is suitable for understanding thermal constraints on clay mineralization because the wall rock is homogeneous and its thermal history well defined. The results from XRD indicated that the clay minerals in the gouge samples are dioctahedral smectite, kaolinite, and 1*Md* illite, whereas clay fillings in fractures and joints in the intact granite (clay vein) include $2M_1$ illite in addition to dioctahedral smectite and 1*Md* illite. The evolution of clay mineralization is reconstructed as follows: (1) high-temperature hydrothermal alteration of feldspar and biotite produced $2M_1$ illite in clay veins; and (2) alteration accompanied by shearing at a lower temperature resulted in the formation of 1*Md* illite in the gouges. This scenario is consistent with the cooling history of the granite constrained by fission-track, U-Pb, and K-Ar dating methods. K-Ar dating of the clay samples separated into multiple particle-size fractions indicated that the low-temperature alteration leading to the production of 1*Md* illite was dated to ~40 Ma. Based on the cooling history of the granite, the 1*Md* illite formed at temperatures of 60−120ºC. This temperature range was at the lower limit of the range reported in previous studies for faults. The spatial and geometrical relation of the faults studied and their K-Ar ages infer evolution which can be described as extensive development of small-scale faults at ~40 Ma followed by coalescence of the small-scale faults to form a larger, recently reactivated, active fault. The K-Ar ages have not been reset by the recent near-surface fault activity.

Key Words—Fault Gouge, Granite, Hydrothermal Alteration, Illite, K-Ar Dating.

INTRODUCTION

Clay production during the evolution of fault gouge affects both the strength and frictional behavior of faults (Saffer and Marone, 2003; Numelin *et al.*, 2007; Ikari *et al.*, 2009), as well as the permeability structure of fault zones (Faulkner and Rutter, 2001; Solum *et al.*, 2005, 2010). Several methods have been proposed to reveal the neomineralization process of clay minerals in gouge, including radiometric dating for various size fractions, illite-smectite quantification, illite-polytype analysis, fabric-intensity measurement, and electron microscopy (*e.g.* Vrolijk and van der Pluijm, 1999; Yan *et al.*, 2001; Solum *et al.*, 2005; Haines *et al.*, 2009). In particular, K-Ar and $^{40}Ar/^{39}Ar$ dating of authigenic and synkinematic clay minerals (especially illite) have been used to determine the timing of neomineralization induced by brittle faulting (*e.g.* Zwingmann and Mancktelow, 2004; Haines and van der Pluijm, 2008). Physical factors such as temperature and pressure are among the important constraints on neomineralization. Systematic patterns of clay alteration in gouge from low-angle normal faults with widely varying ages and wall-rock compositions were studied by Haines and van der Pluijm (2012) who summarized the temperature range of each alteration. Both the age of authigenic clay minerals in a fault and the time-temperature history of the wall rock must be known to place thermal constraints on clay growth; few studies (*e.g.* Zwingmann *et al.*, 2010b) of this type exist in crystalline rocks, however, because the lithology in and around a fault is often heterogeneous and complicated. Homogeneous wall rock would help in terms of defining the time-temperature history of the wall rock, which is often reconstructed based on thermochronological studies.

The Tsuruga Peninsula of central Japan is an excellent region for investigating fault gouge, especially in terms of better understanding the processes and thermal constraints on the neomineralization of clay in fault gouge, because the wall rock is composed of a single lithology and its thermal history is well defined. The basement rock throughout the entire peninsula consists of the Late Cretaceous Kojaku Granite (Kurimoto *et al.*, 1999). Following geological surveys

* E-mail address of corresponding author:
niwa.masakazu@jaea.go.jp
DOI: 10.1346/CCMN.2016.0640202

conducted as part of safety assessments for nuclear power plants, the Japan Atomic Energy Agency (JAEA, 2010) identified Quaternary activity on the Shiraki-Nyu Fault (Figure 1), and the cooling and exhumation histories of the Kojaku Granite were reconstructed by Sueoka *et al.* (2016) using zircon U-Pb dating and apatite and zircon fission-track (AFT and ZFT, respectively) analyses.

In the present study, XRD analysis including polytype identification, particle-size distribution analysis, and K-Ar dating were performed on several types of fault gouge developed in the Kojaku Granite. One of the gouges sampled was taken from the active Shiraki-Nyu Fault, whereas the other gouge samples were taken from inactive faults. Based on these analyses and the reconstructed cooling histories of the Kojaku Granite, thermal constraints on the neomineralization of clay in the gouges and their relations with fault-zone evolution were discussed.

In addition, clay minerals found in filled fractures or joints in the Kojaku Granite were also studied. Fractures filled with clay minerals, described as "clay veins" (Kitagawa *et al.*, 1981; Kitagawa and Nishido, 1994) occur in quartzo-feldspathic rocks due to hydrothermal alteration (Schleicher *et al.*, 2006a; Bartier *et al.*, 2008). The establishment of hydrothermal circulation accompanied by fracture development facilitated hydrothermal alteration within the granite (Turpault *et al.*, 1992; Nishimoto and Yoshida, 2010). Analysis by XRD of a clay-vein sample was performed to distinguish the effects of secondary faulting events from primary hydrothermal alteration. Based on the analytical results of both fault gouges and clay veins, the origin and evolution of the clay minerals were discussed to elucidate the spatial-temporal relation between brittle faulting and hydrothermal alteration.

GEOLOGIC SETTING

The samples analyzed were collected from fault gouges in the Kojaku Granite in the western part of the Tsuruga Peninsula, central Japan (Figure 1). The Kojaku Granite is a fine- to coarse-grained granite (syenogranite to monzogranite; Sawada *et al.*, 1997). The granite is composed of quartz, K-feldspar, plagioclase, biotite, and minor accessory minerals such as zircon, apatite, monazite, and opaque phases. A zircon U-Pb age of 68.5 ± 0.7 Ma (2σ) is regarded as the age of intrusion of the granite in the study area (Sueoka *et al.*, 2016). Biotite K-Ar ages of the granite are 62.9 ± 3.1 Ma

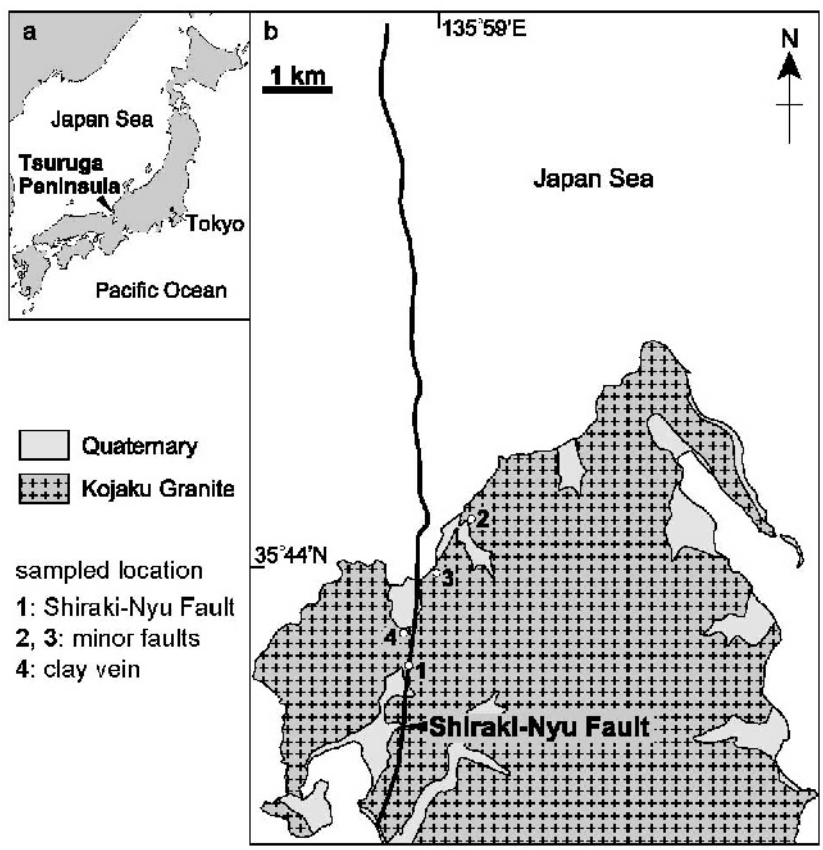

Figure 1. (a) Location of the Tsuruga Peninsula in Japan. (b) Location of the Shiraki-Nyu Fault and the Kojaku Granite within the peninsula. Sampling locations are shown in (b). Base map is from Fukui Prefecture (2010).

https://doi.org/10.1346/CCMN.2016.0640202 Published online by Cambridge University Press

(Kurimoto *et al.*, 1999), 62.0 ± 3.1 Ma, 62.3 ± 1.4 Ma, and 66.7 ± 3.3 Ma (1σ; Sueoka *et al.*, 2016). The AFT and ZFT ages are 51.8 ± 6.5 Ma (1σ) and 70.4 ± 2.0 Ma (1σ), respectively (Sueoka *et al.*, 2016). Based on these age data, fission-track (FT) length analysis, and whole-rock chemical composition analysis, the cooling and exhumation histories of the granite were reconstructed by Sueoka *et al.* (2016), who revealed a three-step process: Late Cretaceous intrusion, then rapid cooling to 180–380ºC by heat conduction (within a few million years or less), followed by slow cooling due to peneplanation beginning at 50–60 Ma.

The north–south striking, east-dipping Shiraki-Nyu Fault cuts the western part of the Tsuruga Peninsula and continues offshore to the north, based on the interpretation of acoustic-sounding data (Figure 1). The estimated total length of the fault is ~15 km (JAEA, 2010). Offshore acoustic surveys also show that upthrust of the east side of the fault occurred in the late Pleistocene or later. The estimated average annual rate of vertical uplift, based on the displacement of middle to late Pleistocene strata, is ~0.2 mm/y. The total vertical displacement of the fault based on the middle Pleistocene strata is 20–30 m. The total displacement prior to the Pleistocene is unknown. Onshore trench excavation and dating of sediments using radiocarbon methods and tephrochronology indicate that the more recent reverse dip-slip movement along the fault occurred at least 9000 y ago (JAEA, 2010).

A few minor faults with shear structures, like faults at locations 2 and 3 as described in the next section, were observed in the study area. Although their length and fault-zone width are incomparably smaller than those of the Shiraki-Nyu Fault, their orientation showing a NNE strike with a steep eastward dip is subparallel to that of the Shiraki-Nyu Fault.

Quartz veins, aplite veins, and pegmatite dikes are commonly observed in the Kojaku Granite. Planar or anastomosing networks of clay veins are developed along these felsic veins and dikes. The clay veins in the Kojaku Granite occur as thin films of clays that fill linear fractures, or anastomosing networks of fractures. The clay veins are pale gray, white, or pale green, and range in thickness from several millimeters to centimeters. The estimated length of each clay vein is several tens of meters or less. These veins are oriented mostly subparallel to joints with subvertical dips in the granite. The most common strike of the subvertical joints is NNE to NE, and a secondary, major orthogonal strike of NW is also found.

DESCRIPTION OF THE SAMPLES

Three fault-gouge samples from different faults were analyzed. The sample at location 1 (35º43’19”N, 135º58’46”E) is from the fault zone of the Shiraki-Nyu Fault. The sample at location 2 (35º44’27”N, 135º59’21”E) is from an inactive minor fault located east of the fast-breeder nuclear reactor known as ‘Monju.’ The sample at location 3 (35º44’01”N, 135º59’00”E) is from a separate inactive fault located south of the Monju site. In addition, a clay sample from a typical clay vein oriented parallel to the quartz veins at location 4 (35º43’35”N, 135º58’42”E) was collected.

Gouge from the Shiraki-Nyu Fault (location 1)

The outcrop of location 1 is along the southern part of the Shiraki-Nyu Fault, where a fault core and adjacent damage zones are present. The fault core is 2–3 m thick in surface outcrop (Figure 2a), and is composed of incohesive cataclasite and fault gouge (Figure 2b; fault-rock terms are consistent with those of Brodie *et al.*, 2007). The damage zones are characterized by granite with a high degree of fracture intensity. The overall thickness of the damage zones is ~25 m.

The cataclasite is characterized by very abundant fractures and granite breccia. Relatively continuous fractures in the cataclasite define an anastomosing foliation that strikes to the north and dips steeply to the east, subparallel to the orientation of the Shiraki-Nyu Fault. The cataclasite is composed mainly of subangular fragments of granite and aplite veins, quartz, feldspar, and biotite in a gray (partly brownish) matrix of finer granitic fragments and clay minerals. Recycled fragments of older granite cataclasite are included in the cataclasite, suggesting the occurrence of multiple cataclastic deformation events (Figure 2c). The aplite and quartz veins occurred prior to the cataclastic

Figure 2 (*facing page*). Photographs of the fault zone of the Shiraki-Nyu Fault at location 1. (a) Outcrop view of the fault zone. Arrows indicate the principal slip surface. (b) Close-up view of the fault core. Yellow arrows indicate the principal slip surface including the planar brownish gouge sampled. Aplite fragments (Ap) are included in the hanging-wall cataclasite. (c) Slice of a sample from the fault core. The reworked clast of cataclasite is cut by a brownish gouge injection (arrow). (d) Eastern margin of the fault core (broken yellow line). Aplite vein (Ap: broken red lines) is cut by the cataclasite of the fault core. Yellow arrows indicate the principal slip surface. (e) Polished slab containing gouge and adjacent cataclasite. Yellow arrows indicate laminae in the gouge. (f) Injection of the brownish gouge. Note convex arcuate foliation in gouge recording drag along injection walls (arrows). (g) Slickenlines with a high-angle pitch on the brownish gouge of the principal slip surface. (h) Slice of a core sample containing gouge and adjacent cataclasite. A composite planar fabric comprising a P foliation and Y shears within the footwall cataclasite indicates a normal dip-slip sense of shear (red arrows). The broken red line shows the location of part g. (i) Slice of a core sample. A composite planar fabric comprising a P foliation and Y shears within the gouge indicates a reverse dip-slip sense of shear (hanging-wall cataclasite is thrust into the top). The gouge materials are injected into the footwall cataclasite (white arrows).

https://doi.org/10.1346/CCMN.2016.0640202 Published online by Cambridge University Press

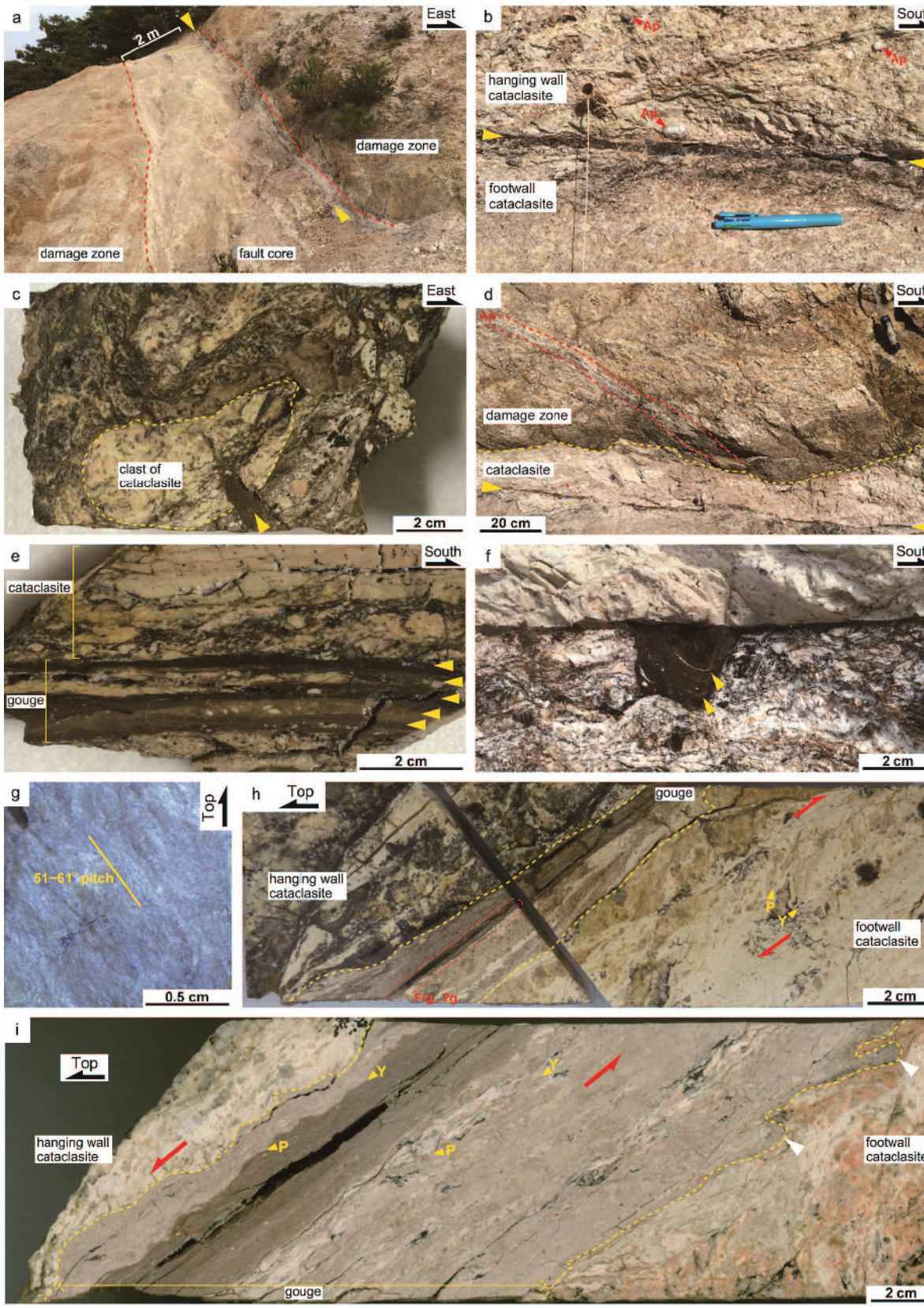

https://doi.org/10.1346/CCMN.2016.0640202 Published online by Cambridge University Press

deformation, because the veins are cut by the cataclasite (Figure 2d) and aplite fragments are included in the fault core (Figure 2b).

Dark brownish fault gouge (<6 cm thick) occurs continuously along the eastern margin of the fault core (Figure 2b). The gouge consists of laminae defined by differences in color intensity which arise from variations in fragment size, density, and mineral content (Figure 2e), indicating an accumulation of shearing along the gouge (*e.g.* Lin *et al.*, 2001; Otsuki *et al.*, 2003). Syntectonic injection or swelling of the gouge materials into the adjacent cataclasite is identifiable in the gouge. The injection breaks and cuts the original cataclsite structure (Figure 2c). The gouge materials are dragged along the injection walls (Figure 2f). This is typical of injection structures accepted as evidence of seismic activity (*e.g.* Lin, 1996; Rowe *et al.*, 2012). The brownish gouge cuts all structures and foliation of the cataclasite. Based on its continuity, and features showing an accumulation of shearing and occurrence of seismic slip, the brownish fault gouge is probably the principal slip surface of the Shiraki-Nyu Fault zone. A sample of the brownish fault gouge was collected for analysis.

The slickenlines along the gouge in outcrops show a dip of north to vertical pitches (Figure 3). In core samples taken from vertical boreholes that penetrate the gouge near location 1, the slickenlines have a moderate to steep plunge (Figure 2g). A composite planar fabric, consisting of a P foliation and Y shears, is well developed in the fault core. Kinematic history within the cataclasite is complicated, because not only reverse faulting but also normal and strike-slip faulting are identified (Figure 2h). In contrast, all observed composite planar fabric in the gouge exhibits a reverse dip-slip sense of shear (Figure 2i). The fault core has sharp contacts with the damage zone (Figure 2d) which contains microcracks but no distinct shear structure is identified and the original equigranular texture is well preserved. The cataclasite and its surrounding granite protolith are affected extensively by hydrothermal alteration characterized by the dissolution, illitization, or chloritization of biotite and the sericitization of feldspar. The hydrothermal alteration is relatively clear in the hanging wall because aplite veins are abundant.

Gouge from a fault located east of the Monju site (location 2)

The fault at location 2 strikes NNE with a steep eastward dip, with a total length of >40 m. Quartz veins subparallel to the fault are present at the site. The fault is marked by a pale green to gray fault gouge 2–20 cm thick (Figure 4a). Slickenlines along the fault plane are sub-horizontal (Figure 3). The fault zone contains a clearly defined composite planar fabric with a dextral strike-slip sense of shear (Figure 4b). Offset on the fault was unknown because a well-defined geologic marker intersecting the fault was not found. Granite fragments, several cm in size, occur within the gouge. The granite bedrock in contact with the gouge is intact and retains its primary equigranular texture in spite of alteration and fracturing (Figure 4b,c). The fracturing is mostly attributed to primary joints and open cracks along quartz or clay veins. An increase of fracture intensity near the gouge is unclear. The alteration is characterized by the sericitization of feldspar, the chloritization, illitization, or dissolution of biotite, and the formation of secondary opaque minerals such as iron oxides. In the altered granite, plagioclase is greenish, while gray translucent quartz and pink K-feldspar retain the same features as in the unaltered equigranular granite (Figure 4d).

The southern end of the fault converges with clay veins in the granite that occur as anastomosing or grid-like fracture networks with clay fillings (Figure 4e). At microscopic scale, clays in the gouge show a partial alignment and define the foliation (Figure 4f), while the clay veins include many fine granite fragments with random alignment (Figure 4g).

Gouge from a fault located south of the Monju site (location 3)

The fault at location 3 is exposed in a stream south of the Monju site. The fault zone is composed of a clay-rich fault core and damage zones either side. The total thickness of the fault zone is ~1 m (Figure 5a). The fault

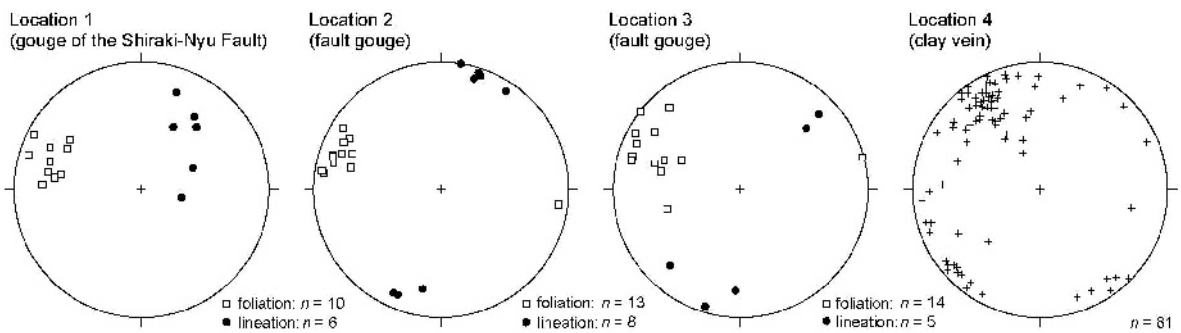

Figure 3. Equal-area lower hemisphere projections showing foliation and lineation in the gouges at locations 1, 2, and 3, and orientations of clay veins in and around location 4.

https://doi.org/10.1346/CCMN.2016.0640202 Published online by Cambridge University Press

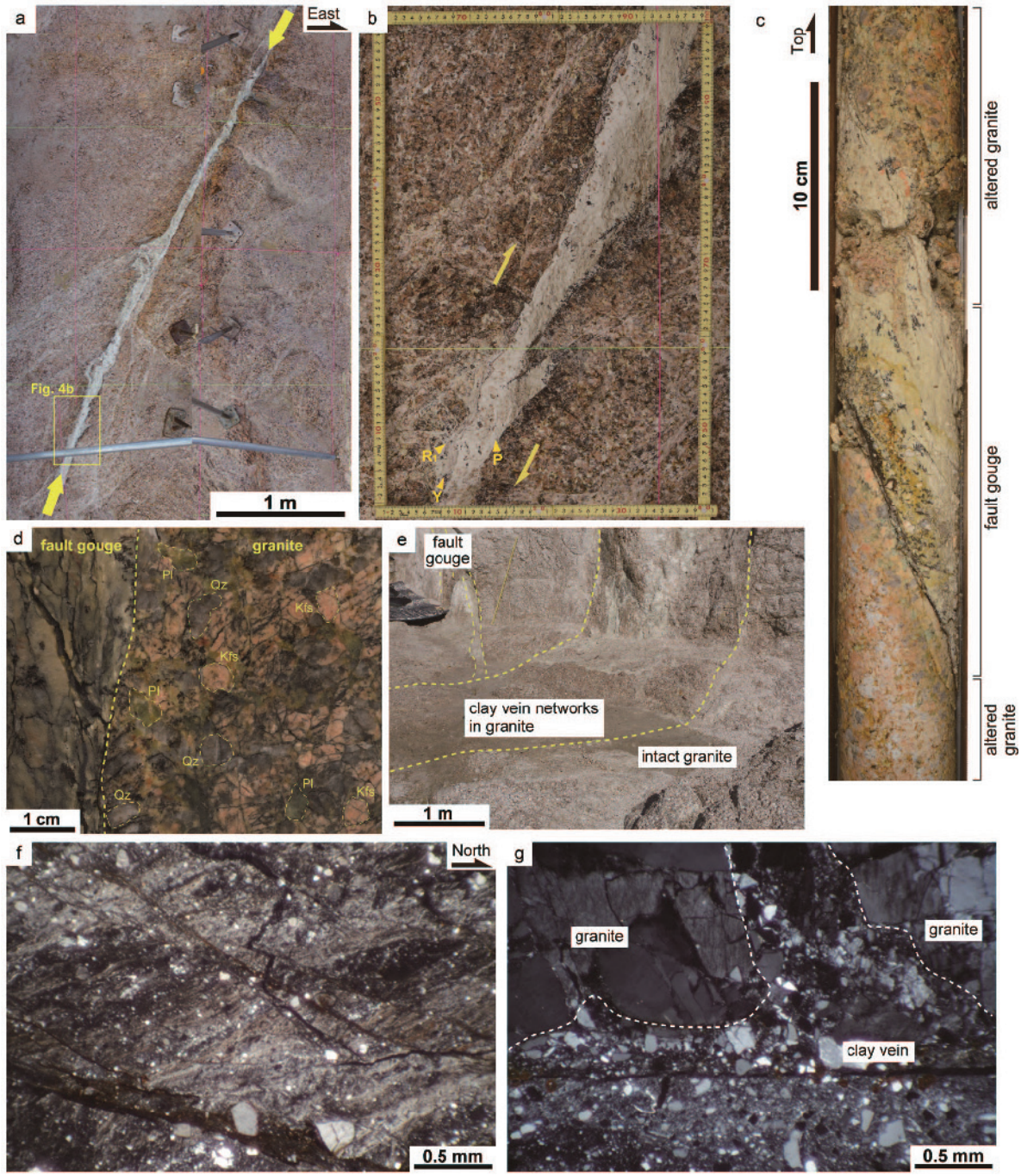

Figure 4. (a) Photograph of the fault (arrows) exposed in the granite bedrock at location 2. Rectangle shows the location of part b. (b) Enlargement of the fault. A composite planar fabric comprising a P foliation, Y shears, and R_1 shears indicates a dextral strike-slip sense of shear. (c) Photograph of the core penetrating the gouge of the fault at location 2. The granite on both sides of the gouge is thoroughly altered; *i.e.* plagioclase is green due to replacement by sericite, and biotite is absent. (d) Polished slab containing gouge and adjacent granite. The granite retains an equigranular texture even though microcracks are pervasive. Translucent quartz (Qz) and pink K-feldspar (Kfs) are relatively unaltered, but plagioclase (Pl) is greenish due to sericitization. Dashed lines indicate grain boundaries. (e) Photograph showing the southern end of the fault converging with clay-vein networks. (f) Photomicrograph of the gouge. Matrix clays are well aligned defining a foliation of N–S trend. Crossed-polarized light. (g) Photomicrograph of the clay vein in part e with a large amount of fine fragments of the host-rock granite origin. Crossed-polarized light.

https://doi.org/10.1346/CCMN.2016.0640202 Published online by Cambridge University Press

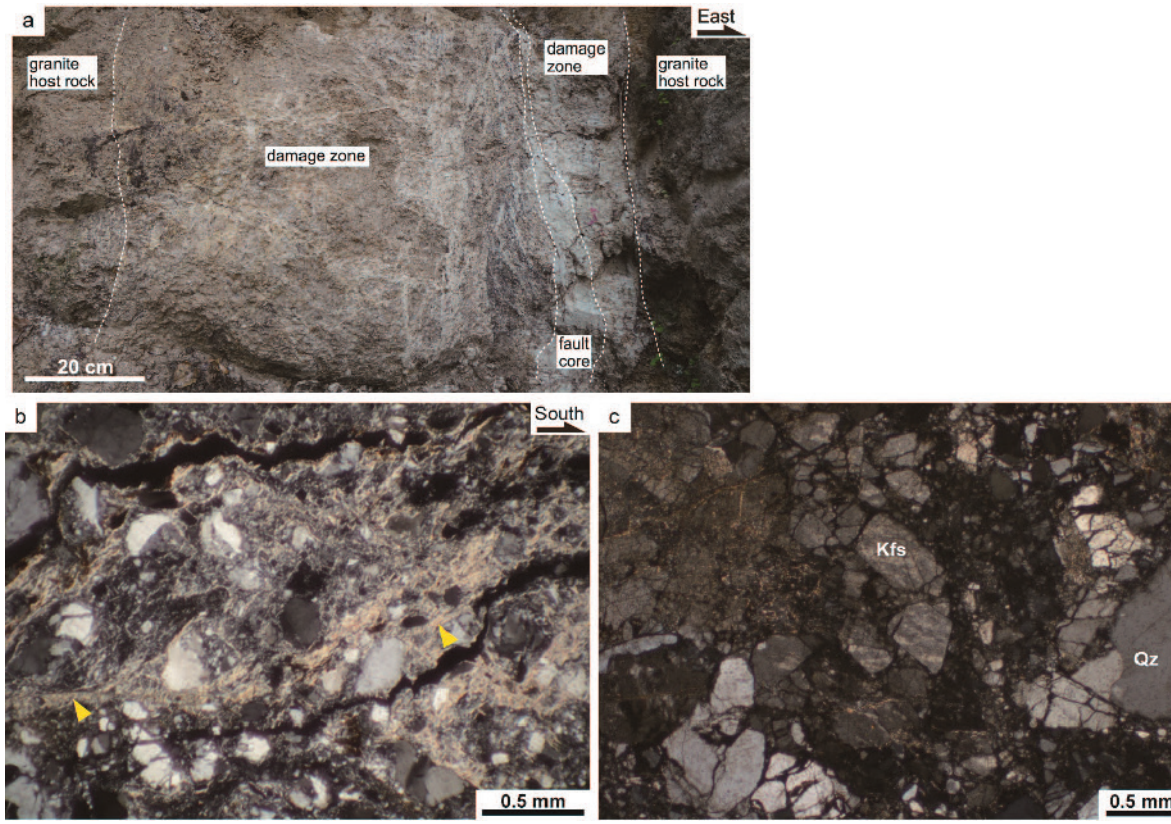

Figure 5. (a) Photograph of the fault zone at location 3. (b) Photomicrograph of the fault core. The matrix clay (arrows) shows a weak alignment of N−S trend. Crossed-polarized light. (c) Photomicrograph of the damage zone. Qz: quartz, Kfs: K-feldspar. Crossed-polarized light.

core consists of a pale gray fault gouge, 2−6 cm thick. A weak foliation defined by an alignment of mineral fragments and a clayey matrix occurs locally in the core (Figure 5b). The damage zone is characterized by anastomosing or grid-like fractures in granite. The fractures in the damage zone are filled with very fine granite fragments and clays of weathering origin (Figure 5c). The fault strikes NNE and dips steeply to the east. The slickenlines along the gouge are sub-horizontal, or plunge gently north or south (Figure 3). Detailed geologic mapping of the fault zone indicates a maximum extent of several hundred meters. The offset on the fault was also unknown here because no well-defined geologic markers intersecting the fault were found. The fault is covered with talus deposits at the southern end of the outcrop. The talus deposits are not displaced by the fault.

Clay vein (location 4)

The clay vein at location 4 is pale gray to green and is exposed along a road cut (Figure 6a). In this outcrop, quartz veins several cm thick are developed in the weathered granite. Locally, the veins are fragmented in a lenticular pattern and are associated with dark gray concentrations of iron-manganese oxides. An anastomosing clay-bearing fracture network, ~30 cm thick, is developed along the quartz veins (Figure 6b). The fractures with clay are not sheared. The observed length of the clay vein is ~30 m. A clay sample, free of granite fragments, was collected from the clay vein in contact with the quartz vein.

The granite adjacent to the clay vein is affected by hydrothermal alteration characterized by the illitization or chloritization of biotite and the sericitization of feldspar (Figure 6c,d). The most common strike of the clay veins in and around location 4 is northeast, and a secondary major strike is northwest (Figure 3). Most of these veins dip subvertically. The sampled vein strikes northeast and dips steeply to the southeast.

METHODS

Sample preparation

Gouge samples from the Shiraki-Nyu Fault at location 1, the fault east of the Monju at location 2, and the fault south of the Monju at location 3 were gently disaggregated using a repetitive freeze-thaw technique (Liewig *et al.*, 1987) to avoid a reduction in size of the minerals and thereby contamination of the finer size fractions with relict K-bearing minerals. To facilitate the

https://doi.org/10.1346/CCMN.2016.0640202 Published online by Cambridge University Press

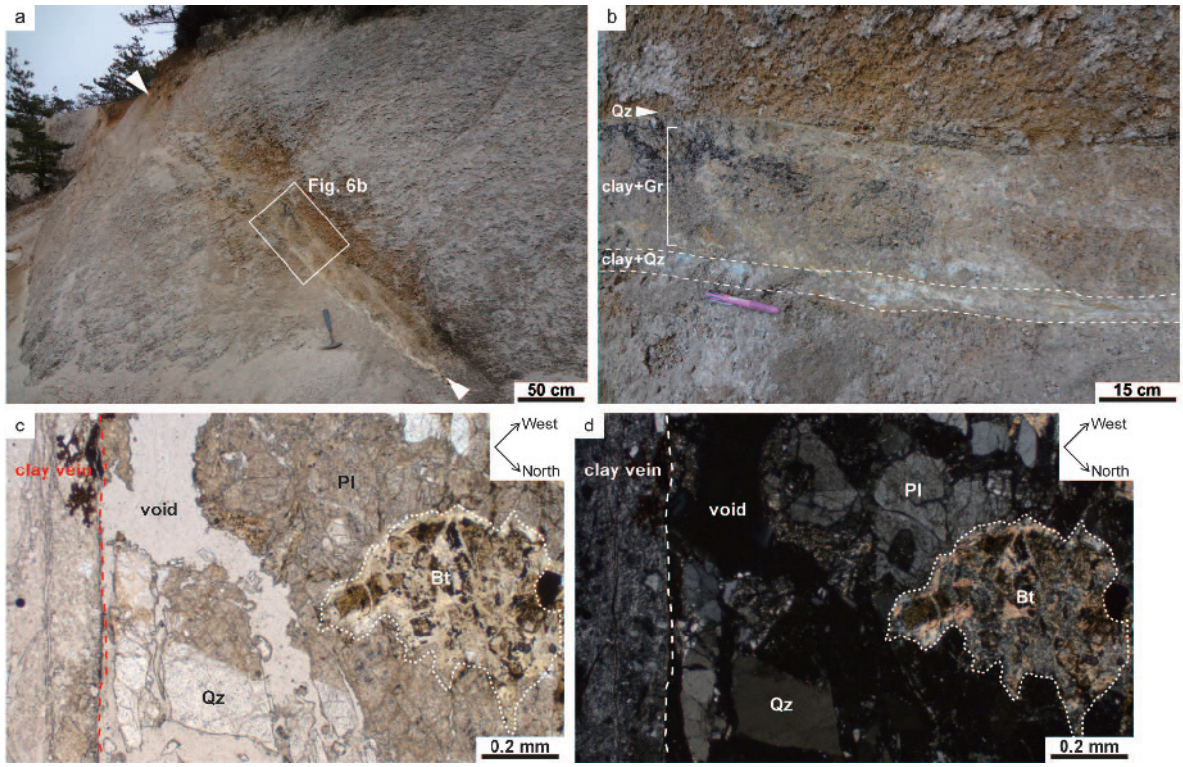

Figure 6. (a) Photograph of a clay vein along with quartz veins in weathered granite at location 4 (white arrows). White rectangle shows the location of part b. (b) Granite with a network-like development of fractures with pale gray to green clay fillings (clay+Gr). Quartz veins, 2–3 cm thick (Qz), are developed on both sides of the granite with clay fillings. A sample was collected from the clay-rich part along a quartz vein in the footwall (clay+Qz). (c) Photomicrograph showing altered granite along the clay vein. Biotite (Bt) is chloritized and illitized along the fractures. Pl: plagioclase, Qz: quartz. Plain-polarized light. (d) Crossed-polarized light version of part c.

freeze-thaw process, samples immersed in deionized water were sealed in Teflon bottles and maintained in a thermostatic bath (Julabo F34, Seelbach, Germany) for 2 weeks at temperatures ranging from −20ºC to 25ºC. From each disaggregated sample, particles of <1 μm in diameter were separated by elutriation according to Stokes' law (Tanner and Jackson, 1947; Williams *et al.*, 1958; Jackson, 2005). The three increasingly fine fractions (<0.1, <0.4, and <1 μm) were further separated using a high-speed centrifuge, based on the modified Stokes' equation (Puretz, 1979; Ross and Morrison, 1988; McFadyen and Fairhurst, 1993; Laidlaw and Steinmetz, 2005). The sample separation into three size fractions using a repetitive freeze-thaw technique allows for the identification of authigenic clay minerals that are abundant in finer fractions, in contrast to primary minerals such as K-feldspar and micas, which are major components of host rocks and generally abundant in coarser fractions. Such careful sample preparation is important to date the brittle faulting adequately (Zwingmann *et al.*, 2010a; Yamasaki *et al.*, 2013).

Particle-size distributions were measured for each fraction with a laser diffraction-scattering particle-size distribution analyzer (HORIBA LA-950V2, Kyoto, Japan; Figure 7) to verify that the separated fractions were actually composed of progressively finer particles. Particle sizes were calculated based on their volumes. The refractive indices of muscovite (1.590) and water (1.333) were used for the calculations.

XRD analysis

Mineral composition was determined by XRD analysis using a Rigaku Ultima IV, Tokyo, Japan, housed at JAEA, with a two-axis goniometer, CuKα radiation, a Kβ filter, and a one-dimensional X-ray detector (D/teX Ultra) at 40 kV and 30 mA, with 0.5º and 10 mm divergence slits, and an 8 mm anti-scattering slit. First, randomly oriented powder films of unaltered bulk granite were analyzed. The bulk granite samples were collected from the bedrock at location 2 and another bedrock outcrop located ~50 m west of the outcrop at location 3. For the analyses of granite powders, each scan ranged from 3 to 70º2θ with a scan rate of 5º2θ min^{-1} and a step size of 0.01º2θ (Figure 8).

For each separated fraction from the gouge samples at locations 1, 2, and 3, both oriented smear mounts to identify clay phases, and randomly oriented powder films to determine the illite polytype (Bailey, 1980,

https://doi.org/10.1346/CCMN.2016.0640202 Published online by Cambridge University Press

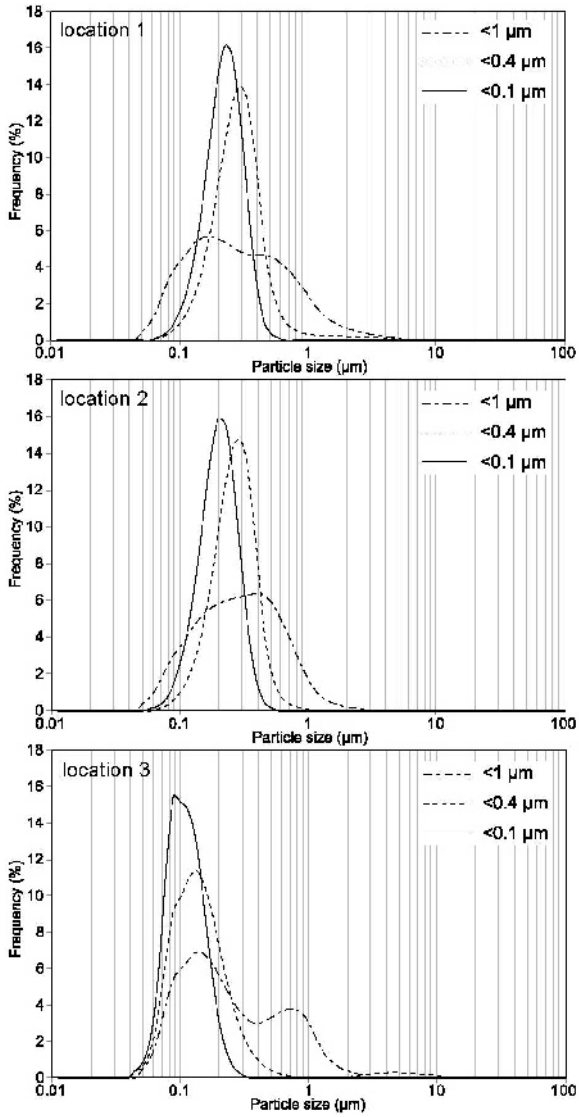

Figure 7. Results of particle-size analysis.

1984) and smectite structure (di or trioctahedral) were analyzed. The oriented samples were treated with ethylene glycol (EG) to help in the identification of smectite. For the illite-polytype analysis and subsequent K and Ar measurements, the remaining suspension of each fraction was dried at 40ºC for two days. Dried solids were crushed gently to powder in an agate mortar.

An oriented smear slide and randomly oriented powder film were analyzed for the clay-vein sample from location 4. To make the smear slide, a suspension of particles <2 μm in diameter was separated by elutriation from a sample immersed in deionized water. A powder film was prepared by pulverization of the bulk dried clay sample using an agate ball mill. In addition, oriented smear slides were analyzed for the cataclasite matrix at location 1 to compare the mineralogy between the cataclasite and gouge. Three samples were collected from the cataclasite matrix from the eastern end, center, and western end of the fault core. A suspension of <2 μm particles was used for the analysis.

For analysis of the oriented smear slides, each scan ranged from 3 to 40º2θ with a scan rate of 0.5º2θ min^{-1} and a step size of 0.01º2θ (Figures 9, 10). For the polytype analyses of randomly oriented powder films, each scan ranged from 16 to 44º2θ with a scan rate of 0.1º2θ min^{-1} and a step size of 0.01º2θ (Figure 11). The scan of the smectite (060) peak ranged from 57 to 64º2θ with a scan rate of 0.1º2θ min^{-1} and a step size of 0.01º2θ (Figure 12). In the present study, the *WILDFIRE*©-software package from Crofton, Maryland (Reynolds, 1993) was used to quantify the amount of $2M_1$ and $1Md$ in the illite mixtures. The procedure to determine the best match between samples and *WILDFIRE*©-calculated patterns was based on the description by Haines and van der Pluijm (2008).

K-Ar dating

K-Ar dating for each separated fraction from the gouge samples at locations 1, 2, and 3 was carried out. Quantitative determination of K concentration was analyzed by flame photometry using an Asahi-Rika FP-33D instrument (Chiba, Japan), housed at the JAEA. The K analytical procedure was based on the work of Matsumoto (1989). Approximately 100 mg of dried and weighed powder was heated and dissolved with a triacid mixture (HF, $HClO_4$, and HNO_3). Lithium was used as the internal standard. The potassium concentration in each fraction was calculated from the mean of two measurements per fraction. Standard deviations of multiple analyses for a standard sample were ~0.5% of the mean. On the other hand, standard deviations of the two measurements of each fraction, *i.e.* half of absolute value of (1^{st}–2^{nd}), were 0.07–2.25% of the mean. Thus, errors in the potassium concentrations were assumed to be 2% of the mean for each fraction.

Ar isotopic ratios were measured using the sensitivity method of Bonhomme *et al.* (1975), employing a Micromass VG5400 mass spectrometer (Manchester, UK), housed at JAEA. Approximately 20 mg of dried powder was wrapped in clean Cu foil, then heated for >2 days in an evacuated holder to remove adsorbed atmospheric Ar from the mineral surfaces. Ar was extracted from the molten samples using a molybdenum crucible in a resistance furnace (Horiguchi Ironworks Ltd., TH-250H, Inami, Hyogo, Japan) at 1500ºC within a vacuum line. After fusion of the sample, the gases released were purified using a Ti-Zr getter and non-evaporable getter pumps. The isotopic composition of Ar was measured using an on-line mass spectrometer employing a Faraday cup. During the course of the study, standard gas of atmospheric composition and a standard sample of SORI93 biotite with a known radiogenic ^{40}Ar volume (Sudo *et al.*, 1998) were also measured. Argon isotopic ratios were calculated based

https://doi.org/10.1346/CCMN.2016.0640202 Published online by Cambridge University Press

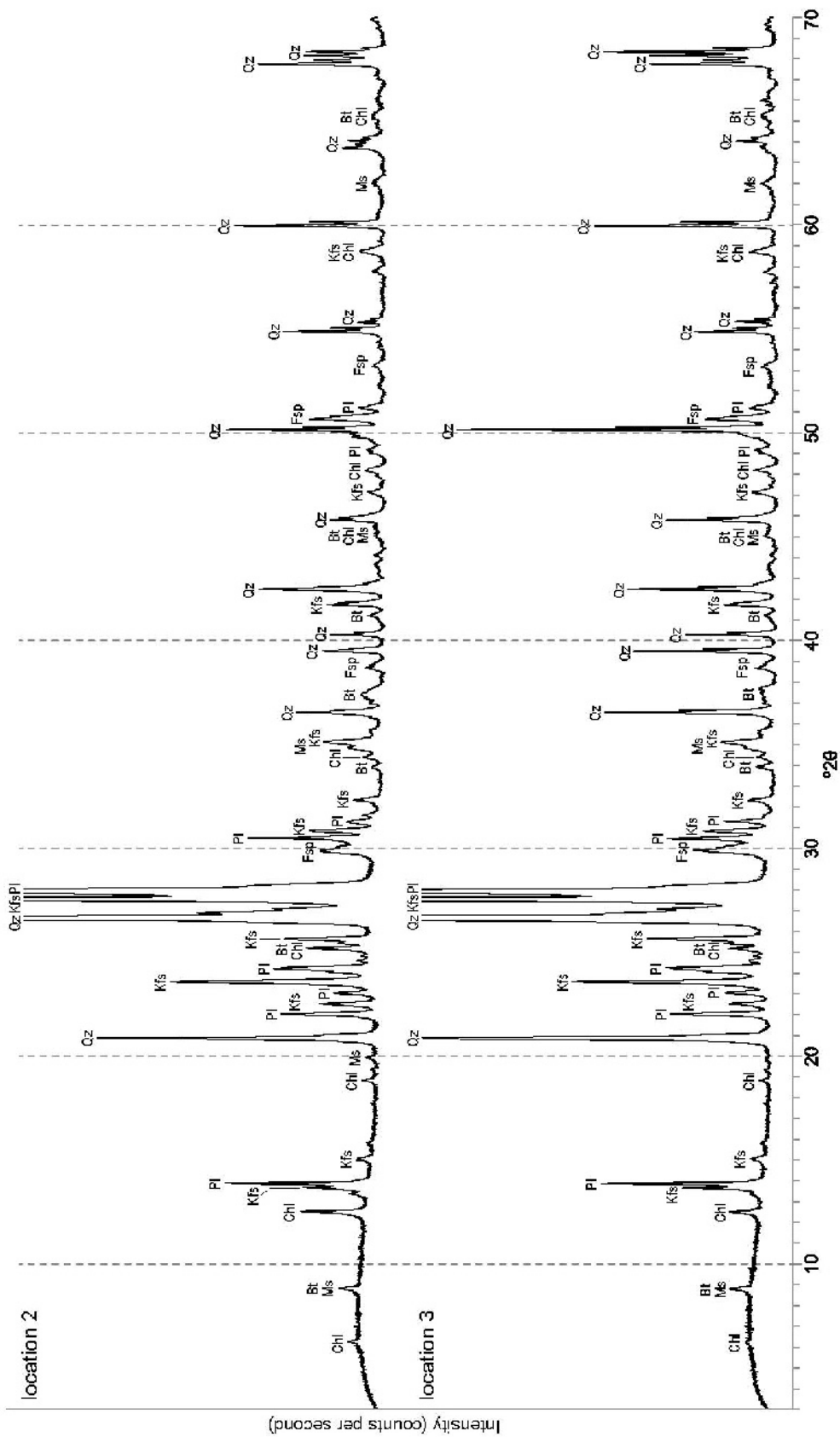

Figure 8. XRD patterns of randomly oriented powder films from the granite host rock. Bt: biotite, Chl: chlorite, Fsp: feldspar, Kfs: K-feldspar, Ms: muscovite, Pl: plagioclase, Qz: quartz.

https://doi.org/10.1346/CCMN.2016.0640202 Published online by Cambridge University Press

on the method reported by Matsumoto *et al.* (1989), Takaoka (1989), and Sudo *et al.* (1996). The decay constants used were those recommended by Steiger and Jäger (1977). The age uncertainties take into account the errors during sample weighing, $^{38}Ar/^{36}Ar$ and $^{40}Ar/^{36}Ar$ measurements, and K analysis. For all measurements in the present study, errors are shown as 2σ. Separation into size fractions for K-Ar dating was not performed for the clay vein at location 4 due to a lack of pure samples.

RESULTS

Mineral identification based on XRD analysis

Based on XRD analyses of randomly oriented powder films from the unaltered bulk granite at locations 2 and 3, the granite is noted to contain abundant quartz, plagioclase, and K-feldspar, and less abundant biotite, muscovite (sericite), and chlorite (Figure 8, Table 1). These minerals were clearly identifiable in thin sections of the Kojaku Granite.

All clay samples included smectite and illite (Figure 9, Table 1). Smectite is present in greater concentrations than illite at all localities. Illite is more abundant in the fault gouge at location 3 and in the clay vein at location 4 than in the gouge samples from locations 1 and 2. Kaolinite, quartz, and K-feldspar were found in the gouge samples, but their amounts decreased with decreasing particle size. Smectite, illite, and kaolinite as well as quartz and feldspar were included in the cataclasite matrix from location 1 (Figure 10). The mineral composition of the cataclasite is similar to that of the gouge. Illite and smectite in all studied samples were generally not interstratified, based on the typical relations between compositions and peak positions for interstratifications of illite and EG-saturated smectite (Reynolds, 1980; Watanabe, 1988). The (060) reflections at 1.50 Å (61.85º) indicate that the smectite was dioctahedral (Figure 12).

The results of analysis of randomly oriented powder films for each fraction of the gouge samples (Figure 11) show the occurrence of a 1*Md* polytype of illite from the following lines of evidence: (1) all fractions had relatively large (020) and 2.58 Å peaks, typical of common illite. (2) An area of broadly elevated intensity between 21 and 31º2θ, defined as an illite hump (Grathoff and Moore, 1996), was identified clearly in all fractions. This outcome is primarily due to the presence of 1*Md* illite. (3) No clear peaks specific to $2M_1$ illite (Moore and Reynolds, 1997) were visible.

The relatively large illite (020) and 2.58 Å peaks, and the clear illite (001) and (002) peaks for oriented analyses, could be attributed to the occurrence of 1*Md* polytypes in all fractions. In particular, the larger illite hump in the gouge at location 3 indicated the dominance of 1*Md* illite as a K-bearing mineral, whereas the <0.1 μm fraction from the gouge lacked K-feldspar.

The 1*Md* polytype of illite was also identifiable from the bulk analysis of the randomly oriented powder film made from the clay vein (Figure 11). In contrast to the gouge samples, peaks specific to $2M_1$ illite were also visible in the clay vein sample. The best-fit model for the calculated XRD patterns, obtained using the *WILDFIRE*© software package, consisted of 55% 1*Md* illite and 45% $2M_1$ illite.

K-Ar ages

The results of K analysis showed that the difference between the repeated K measurements in each fraction for each location was within 2% of the mean, except for the <0.1 μm fraction from location 1 and the <0.4 μm fraction from location 3 (Table 2). Ar isotopic ratios were measured two to three times per fraction. One measurement for the <0.4 μm fraction from location 1 was unsuccessful because sample loading into the vacuum line failed. In addition, one measurement for the <0.1 μm fraction from location 3 was also unsuccessful because Ar

Table 1. Summary of XRD analyses.

Location	Sample	High abundance	Medium abundance	Low abundance	Illite polytype
2	Bulk granite at location 2	Qz, Pl, Kfs		Bt, Ms, Chl	
3	Bulk granite at location 3	Qz, Pl, Kfs		Bt, Ms, Chl	
1	Gouge <1 μm	Sme	Ilt, Kln, Qz, Kfs		1*Md*
	Gouge <0.4 μm	Sme	Ilt, Kln, Qz, Kfs		1*Md*
	Gouge <0.1 μm	Sme	Ilt	Kln, Qz, Kfs	1*Md*
	Cataclasite matrix <2 μm	Sme	Ilt, Kln, Qz	Pl, Kfs	
2	Gouge <1 μm	Sme	Ilt, Qz, Kfs	Kln	1*Md*
	Gouge <0.4 μm	Sme	Ilt, Qz, Kfs	Kln	1*Md*
	Gouge <0.1 μm	Sme	Ilt	Kln, Qz, Kfs	1*Md*
3	Gouge <1 μm	Sme, Ilt, Kln	Qz	Kfs	1*Md*
	Gouge <0.4 μm	Sme, Ilt, Kln		Qz, Kfs	1*Md*
	Gouge <0.1 μm	Sme, Ilt		Kln, Qz	1*Md*
4	Bulk clay vein	Sme, Ilt		Qz	$2M_1$, 1*Md*

Bt: biotite, Chl: chlorite, Ilt: illite, Kfs: K-feldspar, Kln: kaolinite, Ms: muscovite, Pl: plagioclase, Qz: quartz, Sme: smectite

https://doi.org/10.1346/CCMN.2016.0640202 Published online by Cambridge University Press

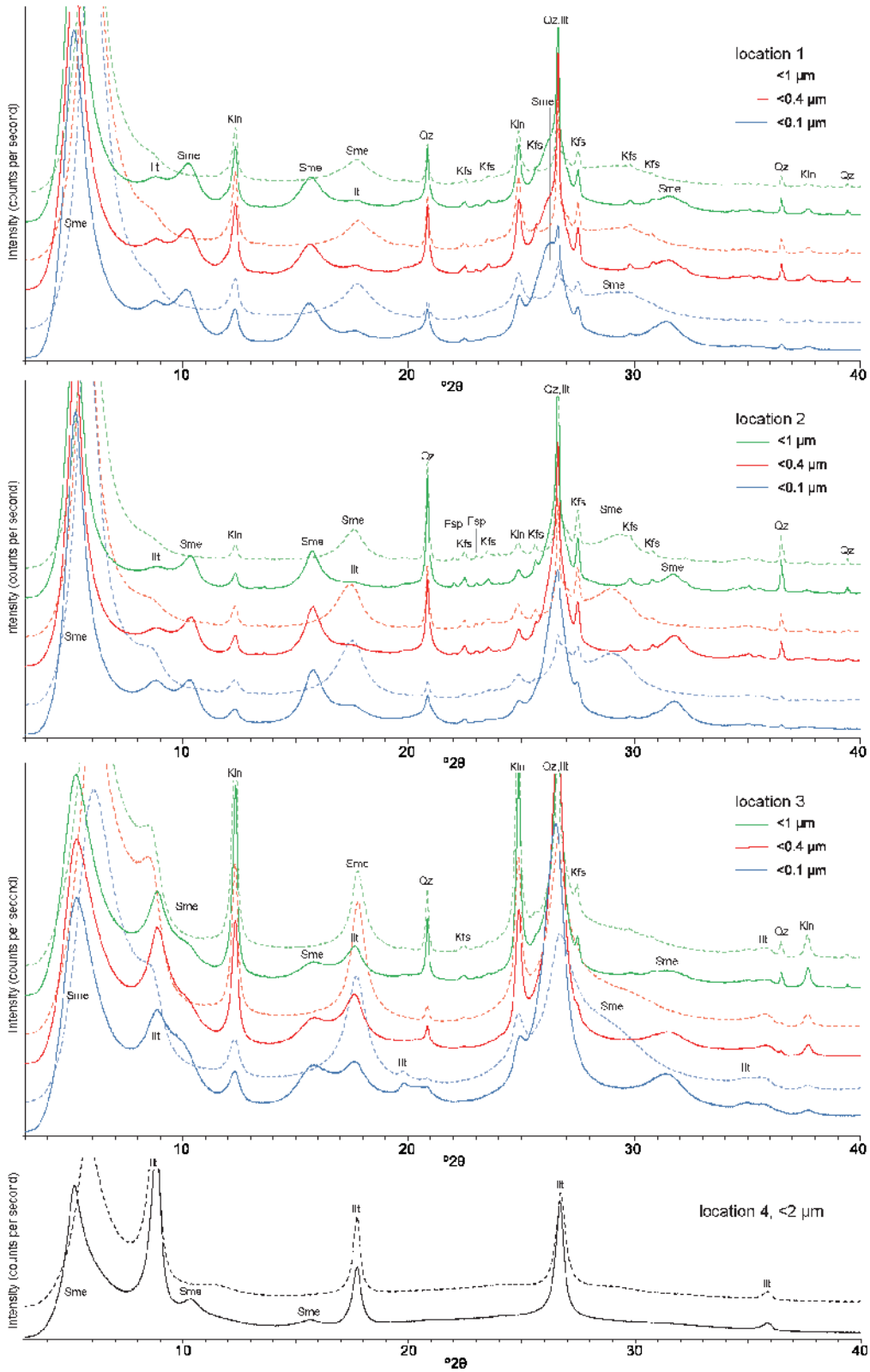

Figure 9. XRD patterns of oriented smear slides for each fraction from gouges at locations 1, 2, and 3, and for <2 μm particles from a clay vein at location 4. Dotted lines are air-dried patterns and solid lines are EG-saturated patterns. Fsp: feldspar, Ilt: illite, Kfs: K-feldspar, Kln: kaolinite, Qz: quartz, Sme: smectite.

https://doi.org/10.1346/CCMN.2016.0640202 Published online by Cambridge University Press

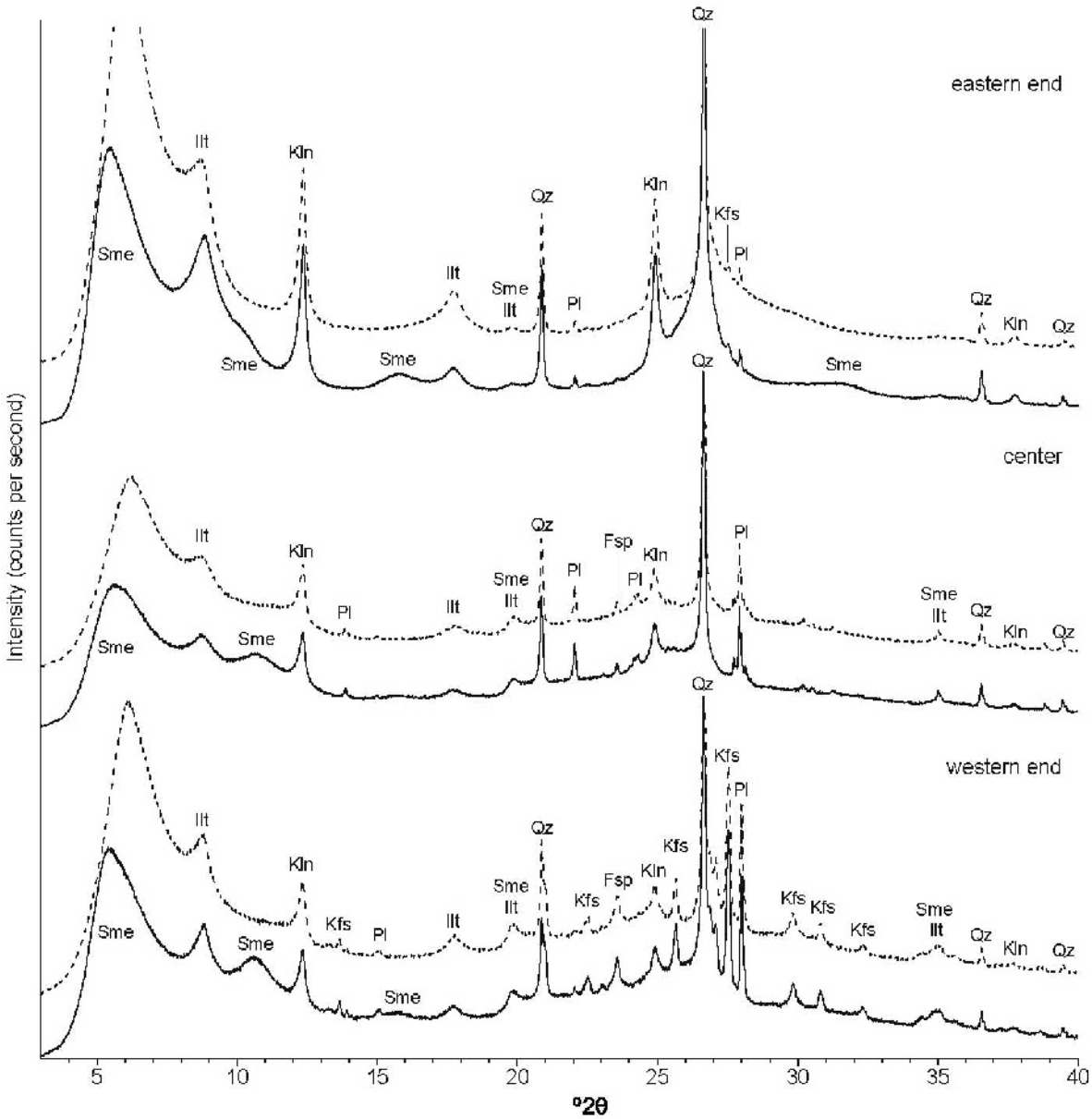

Figure 10. XRD patterns of oriented smear slides for <2 μm particles from the cataclasite matrix at location 1. Dotted lines are the air-dried pattern and solid lines are the EG-saturated pattern. Fsp: feldspar, Ilt: illite, Kfs: K-feldspar, Kln: kaolinite, Pl: plagioclase, Qz: quartz, Sme: smectite.

was dispersed by sample overheating. Results of Ar analysis showed that variations in values within the same fractions and samples were somewhat large (Table 3). Specifically, variations within the <1 μm fraction from location 1 and the <0.4 μm fraction from location 2 were larger than their respective errors. Because the lack of K-feldspar in the <0.1 μm fraction from location 3 suggested that it could provide a more reliable age for the 1*Md* illite, ten measurements were performed for this fraction after dried and powdered samples were stirred carefully in an agate mortar. Seven of the ten Ar measurements were successful. For the K analysis, the difference between maximum and minimum values was within 2.3% of the mean (Table 4). For the Ar analysis, ages for the successful measurements ranged from 40.5 ± 1.6 Ma to 44.0 ± 1.3 Ma (Table 5). Variations between the values were still considerable.

DISCUSSION

Clay mineralogy and the history of hydrothermal alteration

The XRD analyses indicate that illite, smectite, and kaolinite are secondary minerals that formed by altera-

https://doi.org/10.1346/CCMN.2016.0640202 Published online by Cambridge University Press

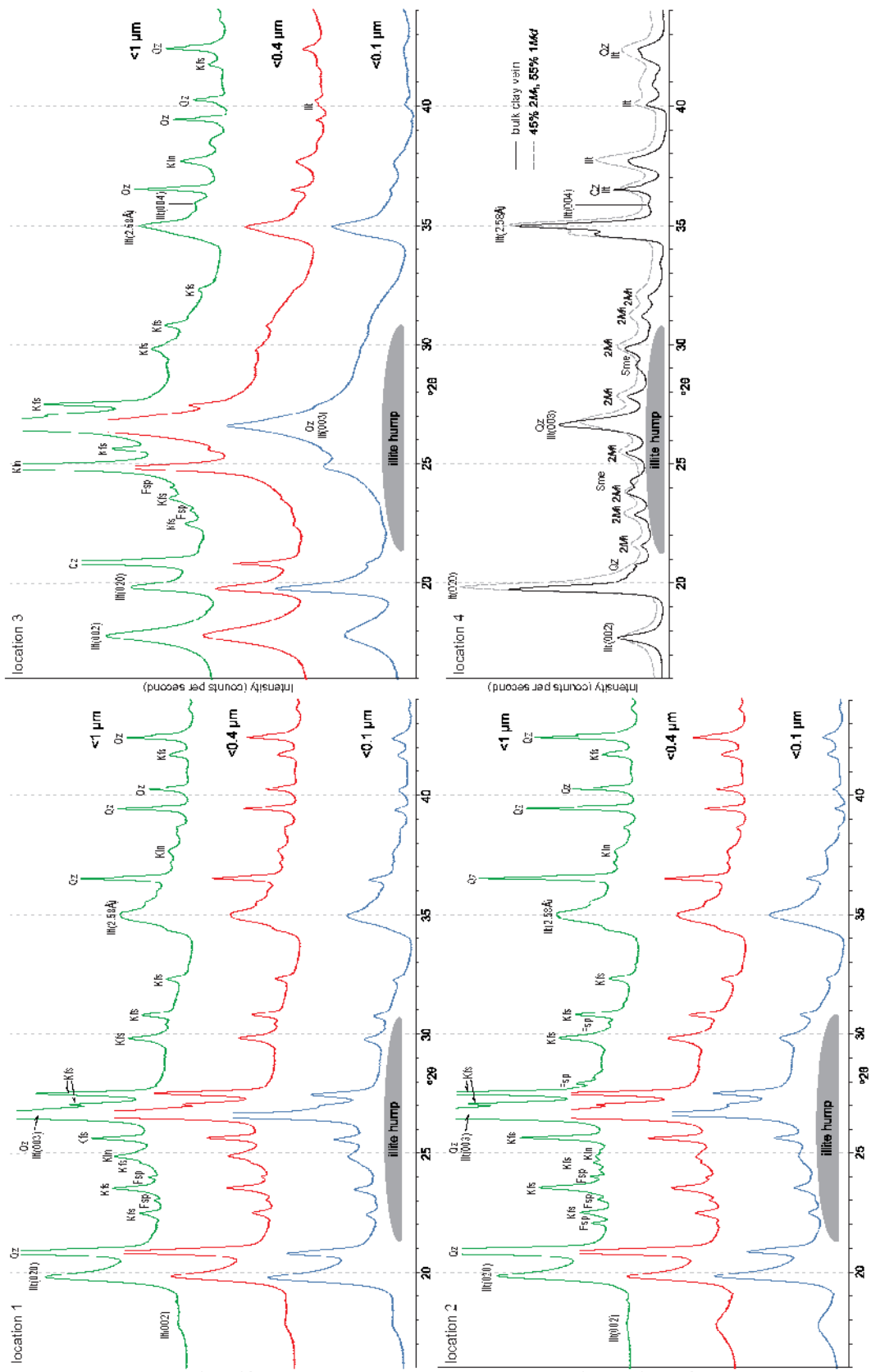

Figure 11. XRD patterns of randomly oriented powder films from each clay fraction from gouges at locations 1, 2, and 3, and from the bulk clay-vein sample in location 4. In the XRD pattern for location 4, the best match calculated using *WILDFIRE*© is also shown (gray broken line). Note that the intensity between 21° and 31° in 2θ is broadly elevated (gray shading), indicating the occurrence of an illite hump in all samples. Fsp: feldspar, Ilt: illite, Kfs: K-feldspar, Kln: kaolinite, Qz: quartz, Sme: smectite, $2M_1$: $2M_1$ illite.

https://doi.org/10.1346/CCMN.2016.0640202 Published online by Cambridge University Press

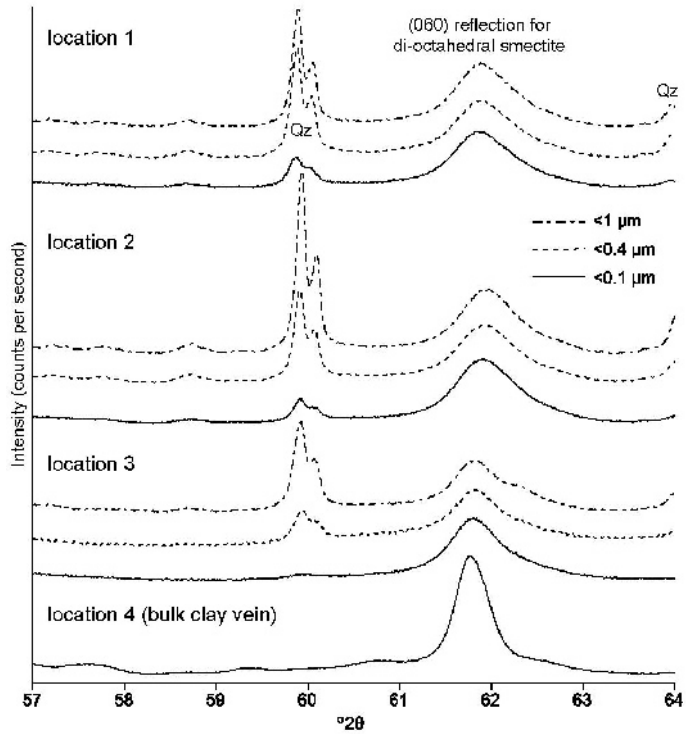

Figure 12. The (060) peaks of smectites from clays sampled in the present study. Qz: quartz.

tion due to the development of fault rocks or clay veins. This follows from the finding that these clay minerals are typically included in the fault rocks and in the clay veins (Figures 9, 10), but have not been detected in the granite host rock (Figure 8).

The XRD analyses of the smear slides indicated that smectite and illite are the main mineral components of the clays within the study area (Figures 9, 12). Polytype analysis of the randomly oriented powder films indicated that both 1*Md*- and $2M_1$-type illites were included in the clay vein, whereas only 1*Md* illite was included in the gouges (Figure 11). Numerous studies have suggested that illite growth is a prograde process in the following order: smectite → 1*Md*/1*M* illite → $2M_1$ illite (Yoder and Eugster, 1955; Velde, 1965; Hunziker *et al.*, 1986; Weaver, 1989); the formation of 1*Md* illite and smectite probably occurred after the formation of $2M_1$ illite in the study area for the following reasons, however. First, no smectite occurred in the granite host rock as a precursor mineral to illite formation (Figure 8). Second, no mixed-layer illite-smectite was identified (Figure 9). If illite and smectite had formed through the same prograde process, mixed-layer illite-smectite should exist along with 1*Md* illite and smectite.

On the other hand, the alteration of feldspar and biotite is also a major trigger of illite formation (Wintsch

Table 2. Results of K analysis for K-Ar age determinations.

Location	Fraction	1st measurement (K_2O, wt.%)	2nd measurement (K_2O wt.%)	Mean (K_2O, wt.%)	Absolute value of ($1^{st}-2^{nd}$)/mean
1	<0.1 μm	1.947	1.997	1.972	0.026*
	<0.4 μm	2.363	2.406	2.384	0.018
	<1 μm	2.545	2.508	2.526	0.015
2	<0.1 μm	3.552	3.517	3.535	0.010
	<0.4 μm	3.817	3.822	3.820	0.001
	<1 μm	3.890	3.915	3.903	0.007
3	<0.1 μm	3.549	3.538	3.543	0.003
	<0.4 μm	4.066	4.253	4.160	0.045*
	<1 μm	4.397	4.427	4.412	0.007

* Absolute value of ($1^{st}-2^{nd}$) is greater than the error for age calculation in this study (>2%).

https://doi.org/10.1346/CCMN.2016.0640202 Published online by Cambridge University Press

Table 3. Results of Ar analysis and calculated K-Ar ages for each sample.

Location	Fraction	K_2O (wt.%)	Radiogenic ^{40}Ar ($10^{-8}cm^3STP/g$)	K-Ar age (Ma)	Non-radiogenic ^{40}Ar (%)
1	<0.1 μm	1.97±0.04	262.6±3.1	40.8±1.0	53.31
			250.7±3.0	39.0±0.9	52.78
	<0.4 μm	2.38±0.05	381.0±4.3	48.8±1.1	32.23
	<1 μm	2.53±0.05	415.3±4.8	50.2±1.2	39.35
			382.7±4.4	46.3±1.1	42.37
2	<0.1 μm	3.54±0.07	515.2±6.1	44.6±1.0	40.52
			513.0±6.1	44.4±1.0	26.86
			498.2±5.7	43.1±1.0	38.93
	<0.4 μm	3.82±0.08	637.5±7.2	51.0±1.2	18.55
			633.5±7.2	50.6±1.2	24.29
			576.2±6.5	46.2±1.1	18.35
	<1 μm	3.90±0.08	665.4±7.7	52.0±1.2	32.31
			638.2±7.3	50.0±1.2	27.29
	<0.1 μm	3.54±0.07	454.4±5.6	39.3±0.9	52.11
3	<0.4 μm	4.16±0.08	643.6±7.4	47.3±1.1	41.70
			628.1±7.2	46.2±1.1	41.51
	<1 μm	4.41±0.09	748.8±8.6	51.8±1.2	35.87
			725.4±8.3	50.2±1.2	38.45
SORI93 (this study)		8.16±0.04*	2500±29	92.49±1.17	6.36
			2580±28	92.61±1.14	2.96
SORI93 reported by Sudo *et al.* (1998)**		8.16±0.04	2500±10	92.6±0.6	

* For the K-Ar age calculation, K_2O data were referred to the value by Sudo *et al.* (1998).
** For the measurements by Sudo *et al.* (1998), errors are reported as 1σ.
STP: standard temperature and pressure

et al., 1995). In the area studied, plagioclase and biotite were altered strongly along the granite−gouge contact and in the clay veins. The altered plagioclase is greenish due to sericitization, and the dark gray biotite has illitized, chloritized, or dissolved (Figures 4c,d, 6c,d). The formation of $2M_1$ illite in the clay veins could thus be controlled mainly by the alteration of feldspar and biotite instead of the prograde alteration from smectite.

Several studies have proposed a retrograde process for illite formation, *i.e.* $2M_1$ illite → $1Md/1M$ illite (Nieto *et al.*, 1994; Zhao *et al.*, 1999; Abad *et al.*, 2003; Schleicher *et al.*, 2006b; Bense *et al.*, 2014). On the other hand, Haines and van der Pluijm (2012) documented the formation of $1Md$ illite from K-feldspar as well as from $2M_1$ illite. The gouges from locations 1, 2, and 3 include $1Md$ illite and K-feldspar but lack $2M_1$ illite. The $1Md$ illite is typically found in all size fractions, while K-feldspar decreases in abundance as the size fraction decreases (Figure 11). These characteristics indicate that the $1Md$ illite in the gouges grew from the breakdown of fragmented K-feldspar, as documented by Haines and van der Pluijm (2012). In contrast, the clay vein at location 4 is characterized by the coexistence of $1Md$ and $2M_1$ illites and the absence of K-feldspar. The illite composition in the clay vein is probably explained by the retrograde transformation of high-temperature $2M_1$ into low-temperature $1Md$ illite, consistent with the studies mentioned above.

The fault core of the Shiraki-Nyu Fault cuts aplite and quartz veins (Figure 2b,d) while the clay vein is

Table 4. Results of repeated K_2O measurements of the <0.1 μm fraction from location 3.

1st wt.%	2nd wt.%	3rd wt.%	4th wt.%	5th wt.%	6th wt.%	7th wt.%	8th wt.%	9th wt.%	10th wt.%	Mean wt.%	SD	(max−min)/mean
3.259	3.287	3.324	3.274	3.270	3.270	3.271	3.262	3.248	3.261	3.273	0.021	0.023

SD: standard deviation

https://doi.org/10.1346/CCMN.2016.0640202 Published online by Cambridge University Press

Table 5. Results of repeated Ar measurements of the <0.1 μm fraction from location 3.

Number	K_2O (wt.%)	Radiogenic ^{40}Ar (10^{-8} cm^3 STP/g)	K-Ar age (Ma)	Non-radiogenic ^{40}Ar (%)
1		452.2±10.9	42.3±1.3	48.97
2		456.4±9.3	42.7±1.2	51.24
3		470.7±10.8	44.0±1.3	47.36
4	3.27±0.07	433.1±14.5	40.5±1.6	47.82
5		439.9±14.9	41.2±1.6	48.36
6		468.9±11.6	43.8±1.4	44.46
7		459.3±12.1	42.9±1.4	46.01
SORI93	8.16±0.04*	2488±28	92.0±1.1	8.45

* For the K-Ar age calculation, K_2O data were referred to the value by Sudo *et al.* (1998).
STP: standard temperature and pressure

developed along quartz veins (Figure 6b). The cataclasite in the fault core has similar mineral composition to the gouge (Figure 10). Based on the low illite crystallinity, indicated by the broad illite peaks in XRD patterns, most illite in the cataclasite matrix could be 1*Md*. These findings suggest that the activities of the gouges associated with the formation of 1*Md* illite clearly followed the development of aplite and quartz veins and subsequent clay-vein development associated with the formation of $2M_1$ illite.

The cooling history of the granite in the study area, based on analyses by FT, U-Pb, and K-Ar analyses, involved a two-step process: rapid cooling to 180−380ºC a few million years or less after intrusion during the Late Cretaceous, followed by slow cooling over 50−60 Myr (Sueoka *et al.*, 2016; Figure 13). $2M_1$ illite generally grows at temperatures >~280ºC (Yoder and Eugster, 1955; Velde, 1965; Środoń and Eberl, 1984), although several cases have been reported where $2M_1$ illite formed at temperatures slightly >125ºC during burial diagenesis in a sedimentary basin (*e.g.* Clauer and Liewig, 2013). In contrast, 1*Md* illite can crystallize at temperatures <~200ºC (Velde, 1965). Specifically, authigenic 1*Md* illite growth in a fault zone appears likely at <180ºC (Haines and van der Pluijm, 2012). The formation of $2M_1$ illite and clay veins involved with the hydrothermal alteration of feldspar and biotite could have occurred during or shortly after the rapid cooling stage. The synfaulting alteration indicated by 1*Md* illite corresponds to the slow cooling stage.

The (060) peak scans indicated that smectite in the studied samples was dioctahedral (Figure 12). Authigenic dioctahedral smectite is commonly found in faults that cut acid volcanics or plutonic rocks (Haines and van der Pluijm, 2012). Smectite crystallizes at <~135ºC (Surdam *et al.*, 1989; Eberl, 1993; Pollastro, 1993; Inoue, 1995; Aplin *et al.*, 2006). Smectite can crystallize independently when interacting with K-depleted fluids, while K-rich fluids initiate illite crystallization. Post-faulting authigenic mineralization of smectite was distinguished (Solum *et al.*, 2003) from synfaulting authigenic mineralization of mixed-layer illite/smectite on the basis of microscopic analysis of fault-rock samples from the Punchbowl fault, southern California. This has also been confirmed by more recent studies of samples from the San Andreas Fault Observatory at Depth (Solum and van der Pluijm, 2004). Dioctahedral smectite from the studied area could be also the product of post-faulting near-surface weathering-related alteration. In contrast, trioctahedral smectite, derived from Mg-rich minerals such as biotite and chlorite, is absent from both the clay veins and gouges (Figure 12). Biotite could possibly have been consumed in the formation of $2M_1$ illite in the clay veins, but the temperatures were too high for smectite to exist stably when forming $2M_1$ illite.

Clay samples from locations 1, 2, and 3 include kaolinite. The reaction of plagioclase and white mica to produce kaolinite is well documented and is particularly well known from the hydrothermal or supergene alteration of granite (Robertson and Eggleton, 1991; Wintsch *et al.*, 1995). Key factors controlling this reaction are temperatures of <120ºC, high fluid-to-rock ratios, and acidic conditions attributed to meteoric water. Thus, kaolinite formation in the clays studied probably occurred as a result of near-surface alteration of gouge clay minerals, similar to the formation of dioctahedral smectite.

Implications of K-Ar ages for the gouges

The K-Ar ages of the gouges (Figure 14) are clearly younger than the reported K-Ar ages for biotite (66.7−62.0 Ma) of the granite host rock (Kurimoto *et al.*, 1999; Sueoka *et al.*, 2016). Major K-bearing minerals in these gouges are 1*Md* illite and K-feldspar. K-feldspar increases in abundance as the size fraction increases (Figures 9, 11), while samples of the coarser <0.4 and <1 μm fractions from the same location yielded older K-Ar ages than those of the finest <0.1 μm fraction (Figure 14). The older ages in the coarser fractions were probably affected by the occurrence of primary

https://doi.org/10.1346/CCMN.2016.0640202 Published online by Cambridge University Press

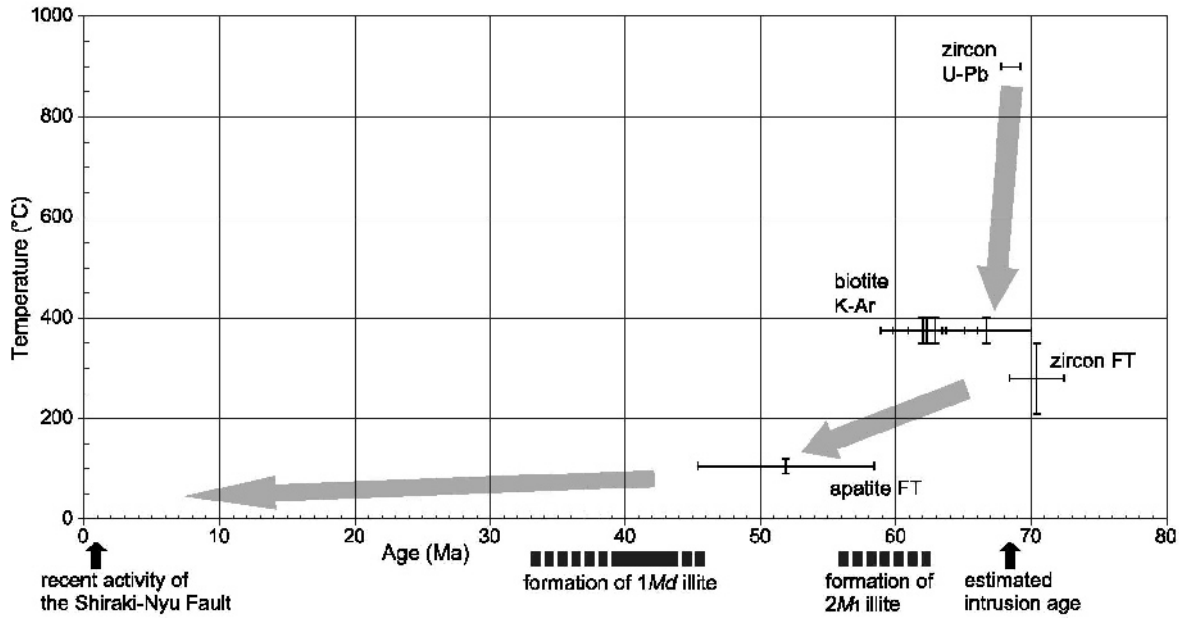

Figure 13. Plots of thermometric age *vs*. closure temperature (Sueoka *et al.*, 2016) and correlation between major hydrothermal and tectonic events and their estimated ages. Large gray arrows show the estimated cooling path of the granite.

K-feldspar, which is present in all of the samples studied except the <0.1 μm fraction from location 3.

In previous studies for fault-gouge dating, calculated quantitative ratios of 1*Md* to $2M_1$ illite for each fraction were plotted *vs*. each K-Ar or $^{40}Ar/^{39}Ar$ age and extrapolated to 0% $2M_1$ (100% 1*Md*) to find the end-member age (*e.g.* Solum and van der Pluijm, 2007; Haines and van der Pluijm, 2008; Zwingmann *et al.*, 2010a). The end-member age is considered to be the age of the authigenic 1*Md* illite formation. For the samples studied, K-feldspar occurs in most fractions as well as illite. It is generally difficult to distinguish K-feldspar quantitatively from 1*Md* illite. The likely cause of this is that the <0.1 μm fraction from location 3, which lacks K-feldspar and $2M_1$ illite, represents the approximate age of 1*Md* illite formation, corresponding to later, low-temperature hydrothermal alteration accompanied by faulting (Figure 13). In this regard, however, errors in the age determinations are largely dependent on the reliability of the illite compositional analysis as well as Ar dating uncertainties. An absolute precision of 2−5% has been reported for the polytype quantitative estimation (Grathoff and Moore, 1996). Thus, the ages of the <0.1 μm fraction from location 3 are also likely to be

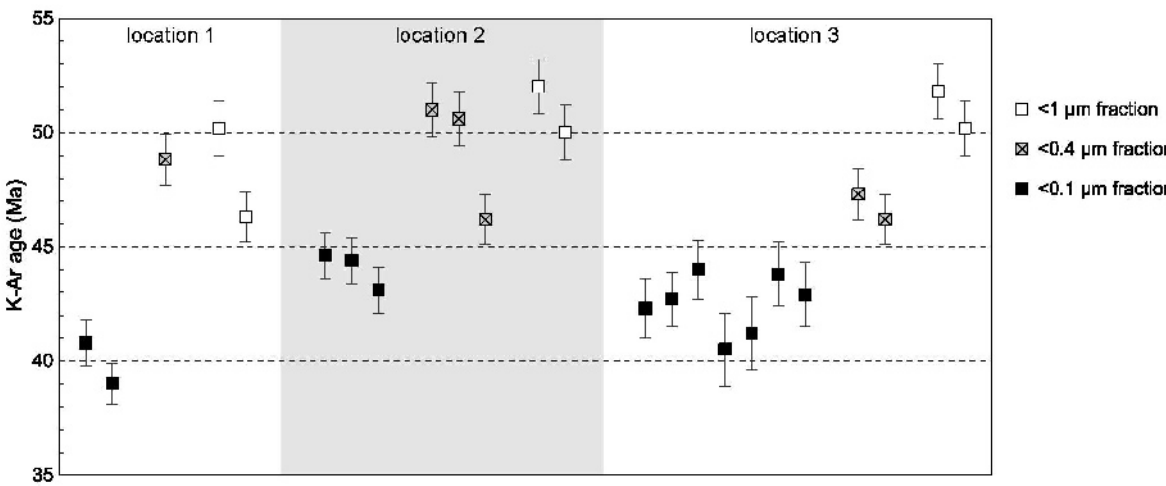

Figure 14. Plots of K-Ar age *vs*. fraction size. The age data obtained from repeat measurements (Table 5) are used for the <0.1 μm fraction from location 3.

https://doi.org/10.1346/CCMN.2016.0640202 Published online by Cambridge University Press

mixing ages, even if they are dominated by the age of the 1*Md* illite. In addition, contamination of interlayer potassium ions in smectite could be a possible cause of the age variations, because the samples studied are rich in smectite. Although some uncertainties remain in terms of an interpretation of the calculated ages, the <0.1 μm fraction from location 3 shows the nearest age of 1*Md* illite formation in all fractions.

A previous thermochronological study of the Kojaku Granite (Sueoka *et al.*, 2016) indicates that the 1*Md* illite formed when the granite temperature was 60−120ºC (from the lower limit of AFT partial annealing zone to the closure temperature of AFT). Previous studies were reviewed by Haines and van der Pluijm (2012) who suggested that the authigenic 1*Md* illite growth in a fault zone occurred at 90−180ºC, possibly with some occurrences at temperatures as low as 60ºC. The temperature range obtained in the present study is at the lower limit of the range proposed in previous studies. Based on the present geothermal gradient around this area (~35ºC/km; Tanaka *et al.*, 2004), the 1*Md* illite probably formed at depths of 2−4 km.

The <0.1 μm fractions from locations 1 and 2 have ages which are similar to those of the <0.1 μm fraction from location 3, even though they contain some K-feldspar. One possibility is that each fault has a different 1*Md* illite age, corresponding to different ages of faulting. In this case, the 1*Md* illite ages from locations 1 and 2 could be younger, but their <0.1 μm fraction ages could be older than the true ages and similar to that of the <0.1 μm fraction from location 3 owing to the mixing of primary K-feldspar. Specifically, the estimated fault length and fault-zone thickness of the Shiraki-Nyu Fault are considerably larger than those at locations 2 and 3. One principal model of fault-zone evolution is that initial, extensive small-scale faults coalesce subsequently to form larger ones (Cox, 2007; Willson *et al.*, 2007; Niwa *et al.*, 2011). The minor faults at locations 2 and 3 have a similar trend of foliation to that of the Shiraki-Nyu Fault (Figure 3). These minor faults are located near the Shiraki-Nyu Fault (within 1 km) considering its total overall length (~15 km). The Shiraki-Nyu Fault experienced many more significant earthquakes over longer periods, whereas the minor faults at locations 2 and 3 could have ceased their activities a short time after initiation.

Nevertheless, K-Ar ages of the fault gouge of the active Shiraki-Nyu Fault are significantly older than the age of recent movements of the fault, as indicated by trench excavations. K-Ar dating may be unable to resolve the timing of near-surface fracturing, at least in the study area. This indicates that illite growth requires appropriate thermal conditions, a suitable wall rock including parental K-bearing minerals, and a trigger (*e.g.* faulting) to overcome the kinetic reaction barrier (Vrolijk and van der Pluijm, 1999; Haines and van der Pluijm, 2012).

CONCLUSIONS

The present study described in-depth analyses of fault gouges from the active Shiraki-Nyu Fault (location 1), the inactive faults east and south of the Monju site (locations 2 and 3), and clay-filled fractures along quartz veins (clay vein; location 4) in the Kojaku Granite of central Japan. Analysis by XRD and K-Ar dating of clays from the homogeneous bedrock having well known cooling and exhumation histories based on thermochronogical studies provided better understanding of the relationship of clay mineralization with alteration and faulting. The findings and their implications are as follows:

(1) Analyses by XRD revealed that the clay samples contained dioctahedral smectite, illite, and kaolinite as secondary minerals, but no mixed-layer illite-smectite. Polytype analysis indicated that both 1*Md* and $2M_1$-type illites were included in the clay vein, whereas only 1*Md* illite was included in fault gouge samples from locations 1, 2, and 3. Based on both field and microscopic observations, the formation of $2M_1$ illite in the vein may have resulted from the hydrothermal alteration of feldspar and biotite at higher temperatures, during or shortly after the rapid cooling stage of the granite. The 1*Md* illite in the gouges may have formed from the breakdown of K-feldspar due to low-temperature hydrothermal alteration with shearing, corresponding to the slow cooling stage. Growth of 1*Md* illite in the vein may have resulted from the transformation of the existing $2M_1$ illite. The dioctahedral smectite and kaolinite were formed as a result of near-surface weathering-related alteration.

(2) K-Ar dating of three increasingly fine fractions (<0.1, <0.4, and <1 μm) from the gouge samples showed that the K-Ar age of the coarser fraction is slightly older than that of the finer fraction due to the presence of primary K-feldspar. In the <0.1 μm fraction from location 3, 1*Md* illite was the major K-bearing mineral, while K-feldspar and $2M_1$ illite were not detected. This suggests that the low-temperature alteration, accompanied by faulting, occurred at ~40 Ma. Based on the cooling history of the granite, the growth of 1*Md* illite occurred when the temperature of the surrounding host rock was 60−120ºC. This temperature range is at the lower limit of the range reported in previous works. Combination of thermochronological studies of the host rock and K-Ar dating with detailed XRD analysis for the fine clay fractions made it possible to place thermal constraints on the clay growth.

(3) Based on the K-Ar ages and clay mineralogy of the fault gouges, and their spatial and geometrical relationship, one principal model of their fault-zone evolution is proposed as follows: (i) extensive development of small-scale faults such as those at locations 2 and 3 at ~40 Ma; and (ii) development of the larger Shiraki-Nyu Fault due to coalescence of the small-scale

https://doi.org/10.1346/CCMN.2016.0640202 Published online by Cambridge University Press

faults. The fault gouge from the active Shiraki-Nyu Fault yields significantly older K-Ar ages than recent movements on the active fault. The K-Ar dating does not appear to be affected by recent near-surface fault activity in the study area.

ACKNOWLEDGMENTS

E. Sasao and G.F. McCrank are thanked for constructive comments which helped to improve the early version of the manuscript. The valuable help of M. Miyazaki and Y. Tanaka with sample preparation, and of K. Yoshikawa and I. Matsui for supporting the XRD analyses, is acknowledged gratefully. A. Stallard is thanked for helping with the language. The present manuscript was improved by the constructive reviews of J.G. Solum, an anonymous reviewer, and by Acting Editor in Chief, M.A. Velbel. The present study was supported partially by a Grant-in-Aid for Scientific Research from the Japan Society for the Promotion of Science (25350500 to M.N. and K.S.).

REFERENCES

Abad, I., Nieto, F., Peacor, D.R., and Velilla, N. (2003) Prograde and retrograde diagenetic and metamorphic evolution in metapelitic rocks of Sierra Espuña (Spain). *Clay Minerals*, **38**, 1–23.

Aplin, A.C., Matenaar, I.F., McCarty, D.K., and van der Pluijm, B.A. (2006) Influence of mechanical compaction and clay mineral diagenesis on the microfabric and pore-scale properties of deep-water Gulf of Mexico mudstones. *Clays and Clay Minerals*, **54**, 500–514.

Bailey, S.W. (1980) Structures of layer silicates. Pp. 1–124 in: *Crystal Structures of Clay Minerals and their X-ray Identification* (G.W. Brindley and G. Brown, editors). Monograph **5**, Mineralogical Society, London.

Bailey, S.W. (1984) Crystal chemistry of the true micas. Pp. 13–60 in: *Micas* (S.W. Bailey, editor). Reviews in Mineralogy, **13**, Mineralogical Society of America, Washington DC.

Bartier, D., Ledésert, B., Clauer, N., Meunier, A., Liewig, N., Morvan, G., and Addad, A. (2008) Hydrothermal alteration of the Soultz-sous-Forêts granite (Hot Fractured Rock geothermal exchanger) into a tosudite and illite assemblage. *European Journal of Mineralogy*, **20**, 131–142.

Bense, F.A., Wemmer, K., Löbens, S., and Siegesmund, S. (2014) Fault gouge analysis: K-Ar illite dating, clay mineralogy and tectonic significance – a study from the Sierras Pampeanas, Argentina. *International Journal of Earth Sciences*, **103**, 189–218.

Bonhomme, M.G., Thuizat, R., Pinault, Y., Clauer, N., Wendling, R., and Winkler, R. (1975) *Méthode de datation potassium–argon. Appareillage et technique*. Notes Techniques de l'Institut de Geologie, Université Louis Pasteur, Strasbourg, France, 53 pp.

Brodie, K., Fettes, D., Harte, B., and Schmid, R. (2007) A systematic nomenclature for metamorphic rocks: 3. Structural terms including fault rock terms. Recommendations by the IUGS Subcommission on the Systematics of Metamorphic Rocks: http://www.bgs.ac.uk/SCMR/docs/papers/paper_3.pdf

Clauer, N. and Liewig, N. (2013) Episodic and simultaneous illitization in oil-bearing Brent Group and Fulmar Formation sandstones from the northern and southern North Sea based on illite K-Ar dating. *Bulletin of the American Association of Petroleum Geologists*, **97**, 2149–2171.

Cox, S.F. (2007) Structural and isotopic constraints on fluid flow regimes and fluid pathways during upper crustal deformation: an example from the Taemas area of the Lachlan Orogen, SE Australia. *Journal of Geophysical Research*, **112**, B08208, doi:10.1029/2006JB004734.

Eberl, D.D. (1993) Three zones for illite formation during burial diagenesis and metamorphism. *Clays and Clay Minerals*, **41**, 26–37.

Faulkner, D.R. and Rutter, E.H. (2001) Can the maintenance of overpressured fluids in large strike-slip fault zones explain their apparent weakness? *Geology*, **29**, 503–506.

Fukui Prefecture (2010) *Geological Map of Fukui Prefecture and its Explanatory Note*. Fukui Prefectural Public Corporation of Construction Technology, Japan, 173 pp.

Grathoff, G.H. and Moore, D.M. (1996) Illite polytype quantification using WILDFIRE© calculated X-ray diffraction patterns. *Clays and Clay Minerals*, **44**, 835–842.

Haines, S.H. and van der Pluijm, B.A. (2008) Clay quantification and Ar-Ar dating of synthetic and natural gouge: Application to the Miocene Sierra Mazatán detachment fault, Sonora, Mexico. *Journal of Structural Geology*, **30**, 525–538.

Haines, S.H. and van der Pluijm, B.A. (2012) Patterns of mineral transformations in clay gouge, with examples from low-angle normal fault rocks in the western USA. *Journal of Structural Geology*, **43**, 2–32.

Haines, S.H., van der Pluijm, B.A., Ikari, M.J., Saffer, D.M., and Marone, C. (2009) Clay fabric intensity in natural and artificial fault gouges: Implications for brittle fault zone processes and sedimentary basin clay fabric evolution. *Journal of Geophysical Research*, **114**, B05406, doi:10.1029/2008JB005866.

Hunziker, J.C., Frey, M., Clauer, N., Dallmeyer, R.D., Friedrichsen, H., Flehmig, W., Hochstrasser, K., Roggwiler, P., and Schwander, H. (1986) The evolution of illite to muscovite: mineralogical and isotopic data from the Glarus Alps, Switzerland. *Contributions to Mineralogy and Petrology*, **92**, 157–180.

Ikari, M.J., Saffer, D.M., and Marone, C. (2009) Frictional and hydrologic properties of clay-rich fault gouge. *Journal of Geophysical Research*, **114**, B05409, doi:10.1029/2008JB006089.

Inoue, A. (1995) Formation of clay minerals in hydrothermal environments. Pp. 269–329 in: *Origin and Mineralogy of Clays* (B. Velde, editor). Springer, Berlin.

Jackson, M.L. (2005) *Soil Chemical Analysis. Advanced Course*, revised 2nd edition. Parallel Press, University of Wisconsin-Madison Libraries, Madison, Wisconsin, USA, 930 pp.

Japan Atomic Energy Agency (2010) Report on the assessment of seismic safety of Monju prototype fast-breeder reactor based on "Regulatory Guide for Reviewing Seismic Design of Nuclear Power Reactor Facilities (New Guideline, Full Revised at 2006)" (revised version in 2010). http://www.jaea.go.jp/04/turuga/jturuga/press/2010/02/p100202.pdf (in Japanese).

Kitagawa, R. and Nishido, H. (1994) Orientation analysis and formation ages of fractures filled with clay minerals (clay veins) in Hiroshima and Shimane Prefectures, Southwest Japan. *Journal of Japan Society of Engineering Geology*, **35**, 60–68.

Kitagawa, R., Kakitani, S., Takeno, S., and Nishida, Y. (1981) Topographical examination and genesis of clay veins found in the Kumogi granite mass in Shimane Prefecture, southwest Japan. *Journal of the Japanese Association of Mineralogists, Petrologists and Economic Geologists*, **76**, 262–272.

Kurimoto, C., Naito, K., Sugiyama, Y., and Nakae, S. (1999) *Geology of the Tsuruga District with Geological Sheet Map at 1:50,000*. Geological Survey of Japan, 73 pp.

Laidlaw, I. and Steinmetz, M. (2005) Introduction to differential sedimentation. Pp. 270–290 in: *Analytical Ultracentrifugation: Techniques and Methods* (D.B. Scott, S.E. Harding, and A.J. Rowe, editors). Royal Society of Chemistry, Cambridge, UK.

Liewig, N., Clauer, N., and Sommer, F. (1987) Rb-Sr and K-Ar dating of clay diagenesis in Jurassic sandstone oil reservoir, North Sea. *Bulletin of the American Association of Petroleum Geologists*, **71**, 1467–1474.

Lin, A. (1996) Injection veins of crushing-originated pseudotachylyte and fault gouge formed during seismic faulting. *Engineering Geology*, **43**, 213–224.

Lin, A., Shimamoto, T., Maruyama, T., Sigetomi, M., Miyata, T., Takemura, K., Tanaka, H., Uda, S., and Murata, A. (2001) Comparative study of cataclastic rocks from a drill core and outcrops of the Nojima fault zone on Awaji Island, Japan. *Island Arc*, **10**, 368–380.

Matsumoto, A. (1989) Improvement for determination of potassium in K-Ar dating. *Bulletin of Geological Survey of Japan*, **40**, 65–70.

Matsumoto, A., Uto, K., and Shibata, K. (1989) K-Ar dating by peak comparison method – New technique applicable to rocks younger than 0.5 Ma. *Bulletin of the Geological Survey of Japan*, **40**, 565–579.

McFadyen, P. and Fairhurst, D. (1993) High-resolution particle size analysis from nanometres to microns. *Clay Minerals*, **28**, 531–537.

Moore, D.M. and Reynolds, R.C. (1997) *X-ray Diffraction and the Identification and Analysis of Clay Minerals*, 2nd edition. Oxford University Press, New York, 378 pp.

Nieto, F., Velilla, N., Peacor, D.R., and Huertas, M.O. (1994) Regional retrograde alteration of sub-greenschist facies chlorite to smectite. *Contributions to Mineralogy and Petrology*, **115**, 243–252.

Nishimoto, S. and Yoshida, H. (2010) Hydrothermal alteration of deep fractured granite: Effects of dissolution and precipitation. *Lithos*, **115**, 153–162.

Niwa, M., Kurosawa, H., and Ishimaru, T. (2011) Spatial distribution and characteristics of fracture zones near a long-lived active fault: A field-based study for understanding changes in underground environment caused by long-term fault activities. *Engineering Geology*, **119**, 31–50.

Numelin, T., Marone, C., and Kirby, E. (2007) Frictional properties of natural fault gouge from a low-angle normal fault, Panamint Valley, California. *Tectonics*, **26**, TC2004, doi:10.1029/2005TC001916.

Otsuki, K., Monzawa, N., and Nagase, T. (2003) Fluidization and melting of fault gouge during seismic slip: identification in the Nojima fault zone and implications for focal earthquake mechanisms. *Journal of Geophysical Research*, **108**, B4, 2192, doi:10.1029/2001JB001711.

Pollastro, R.M. (1993) Considerations and applications of the illite/smectite geothermometer hydrocarbon-bearing rocks of Miocene to Mississippian age. *Clays and Clay Minerals*, **41**, 119–133.

Puretz, J. (1979) Centrifugal particle size analysis and the Joyce–Loebl disc centrifuge. Pp. 77–88 in: *Particle Size Analysis* (J.D. Stockham and E.G. Fochtman, editors). Ann Arbor Science, Ann Arbor, Michigan, USA.

Reynolds, R.C. (1980) Interstratified clay minerals. Pp. 249–304 in: *Crystal Structures of Clay Minerals and their X-ray Identification* (G.W. Brindley and G. Brown, editors). Monograph **5**, Mineralogical Society, London.

Reynolds, R.C. Jr. (1993) WILDFIRE – A computer program for the calculation of three-dimensional powder X-ray diffraction patterns for mica polytypes and their disordered variations. Hanover, New Hampshire, USA.

Robertson, I.D.M. and Eggleton, R.A. (1991) Weathering of granitic muscovite to kaolinite and halloysite and of plagioclase-derived kaolinite to halloysite. *Clays and Clay Minerals*, **39**, 113–126.

Ross, S. and Morrison, E.D. (1988) *Colloidal Systems and Interfaces*. John Wiley & Sons, New York, 440 pp.

Rowe, C.D., Kirkpatrick, J.D., and Brodsky, E.E. (2012) Fault rock injections record paleo-earthquakes. *Earth and Planetary Science Letters*, **335-336**, 154–166.

Saffer, D.M. and Marone, C. (2003) Comparison of smectite- and illite-rich gouge frictional properties: Application to the updip limit of the seismogenic zone along subduction megathrusts. *Earth and Planetary Science Letters*, **215**, 219–235.

Sawada, K., Yoshida, G., and Fujii, R. (1997) Granitic masses around Lake Biwa, southwest Japan: the Koujyaku granite pluton. *Earth Science (Chikyu Kagaku)*, **51**, 401–412.

Schleicher, A.M., Warr, L.N., Kober, B., Laverret, E., and Clauer, N. (2006a) Episodic mineralization of hydrothermal illite in the Soultz-sous-Forêts granite (Upper Rhine Graben, France). *Contributions to Mineralogy and Petrology*, **152**, 349–364.

Schleicher, A.M., Warr, L.N., and van der Pluijm, B.A. (2006b) Fluid focusing and back-reactions in the uplifted shoulder of the Rhine rift system: a clay mineral study along the Schauenburg Fault zone (Heidelberg, Germany). *International Journal of Earth Sciences*, **95**, 19–33.

Solum, J.G. and van der Pluijm, B.A. (2004) Phyllosilicate mineral assemblages of the SAFOD Pilot Hole and comparison with an exhumed segment of the San Andreas Fault System. *Geophysical Research Letters*, **31**, L15S19, doi:10.1029/2004GL019909.

Solum J.G. and van der Pluijm B.A. (2007) Reconstructing the Snake River–Hoback River Canyon section of the Wyoming thrust belt through direct dating of clay-rich fault rocks. *Geological Society of America Special Paper*, **433**, 183–196.

Solum, J.G., van der Pluijm, B.A., Peacor, D.R., and Warr, L.N. (2003) Influence of phyllosilicate mineral assemblages, fabrics, and fluids on the behavior of the Punchbowl fault, southern California. *Journal of Geophysical Research*, **108**, B5, 2233, doi:10.1029/2002JB001858.

Solum, J.G., van der Pluijm, B.A., and Peacor, D.R. (2005) Neocrystallization, fabrics and age of clay minerals from an exposure of the Moab Fault, Utah. *Journal of Structural Geology*, **27**, 1563–1576.

Solum, J.G., Davatzes, N.C., and Lockner, D.A. (2010) Fault-related clay authigenesis along the Moab Fault: Implications for calculations of fault rock composition and mechanical and hydrologic fault zone properties. *Journal of Structural Geology*, **32**, 1899–1911.

Środoń, J. and Eberl, D.D. (1984) Illite. Pp. 495–544 in: *Micas* (S.W. Bailey, editor). Reviews in Mineralogy, **13**, Mineralogical Society of America, Washington DC.

Steiger, R.H. and Jäger, E. (1977) Subcommission on geochronology: convention on the use of decay constants in geo- and cosmochronology. *Earth and Planetary Science Letters*, **36**, 359–362.

Sudo, M., Tagami, T., Sato, K., Hasebe, N., and Nishimura, S. (1996) Calibration of a new Ar analytical system for the K-Ar dating method and analytical results of K-Ar age known samples. *Memoirs of the Faculty of Science, Kyoto University, Series of Geology and Mineralogy*, **58**, 21–40.

Sudo, M., Uto, K., Anno, K., Ishizuka, O., and Uchiumi, S. (1998) SORI93 biotite: A new mineral standard for K-Ar dating. *Geochemical Journal*, **32**, 49–58.

Sueoka, S., Umeda, K., Yasue, K., Niwa, M., Shimada, K., Ishimaru, T., Danhara, T., Iwano, H., and Yagi, K. (2016) Cooling and denudation history of the Tsuruga body of the Kójaku granite, southwest Japan, constrained from multi-

system thermochronology. *Journal of Geography (Chigaku Zasshi)*, **125**, 201–219.

Surdam, R.C., Crossey, L.J., Hagen, E.S., and Heasler, H.P. (1989) Organic-inorganic interactions and sandstone diagenesis. *Bulletin of the American Association of Petroleum Geologists*, **73**, 1–23.

Takaoka, N. (1989) Problems in the K-Ar dating of Quaternary volcanic rocks younger than 1 Ma. *Mass Spectrometry*, **37**, 343–351.

Tanaka, A., Yano, Y., and Sasada, M. (2004) *Geothermal gradient data in and around Japan*. Digital Geoscience Map DGM P-5, Geological Survey of Japan.

Tanner, C.B. and Jackson, M.L. (1947) Monographs of sedimentation times for soil particles under gravity or centrifugal acceleration. *Soil Science Society of America Proceedings*, **12**, 60–65.

Turpault, M.P., Berger, G., and Meunier, A. (1992) Dissolution-precipitation processes induced by hot water circulation in fractured granite. Part 1. Wall-rock alteration and vein deposit processes. *European Journal of Mineralogy*, **4**, 1457–1475.

Velde, B. (1965) Experimental determination of muscovite polymorph stabilities. *American Mineralogist*, **50**, 436–449.

Vrolijk, P. and van der Pluijm, B.A. (1999) Clay gouge. *Journal of Structural Geology*, **21**, 1039–1048.

Watanabe, T. (1988) The structural model of illite/smectite interstratified mineral and the diagram for its identification. *Clay Science*, **7**, 97–114.

Weaver, C.E. (1989) *Clays, Muds, and Shales*. Developments in Sedimentology, **44**, Elsevier, Amsterdam, 818 pp.

Williams, J.W., van Holde, K.E., Baldwin, R.L., and Fujita, H. (1958) The theory of sedimentation analysis. *Chemical Reviews*, **58**, 715–744.

Willson, J.P., Lunn, R.J., and Shipton, Z.K. (2007) Simulating spatial and temporal evolution of multiple wing cracks around faults in crystalline basement rocks. *Journal of Geophysical Research*, **112**, B08408, doi:10.1029/2006JB004815.

Wintsch, R.P., Christoffersen, R. and Kronenberg, A.K. (1995) Fluid-rock reaction weakening of fault zones. *Journal of Geophysical Research*, **100**, 13021–13032.

Yan, Y., van der Pluijm, B.A., and Peacor, D.R. (2001) Deformation microfabrics of clay gouge, Lewis Thrust, Canada: a case for fault weakening from clay transformation. Pp. 103–112 in: *The Nature and Tectonic Significance of Fault Zone Weakening* (R.E. Holdsworth, R.A. Strachan, J.F. Magloughlin, and R.J. Knipe, editors). Special Publications, **186**, Geological Society, London.

Yamasaki, S., Zwingmann, H., Yamada, K., Tagami, T., and Umeda, K. (2013) Constraining the timing of brittle deformation and faulting in the Toki granite, central Japan. *Chemical Geology*, **351**, 168–174.

Yoder, H. and Eugster, H. (1955) Synthetic and natural muscovites. *Geochimica et Cosmochimica Acta*, **8**, 225–280.

Zhao, G., Peacor, D.R., and McDowell, D. (1999) "Retrograde diagenesis" of clay minerals in the Precambrian Freda Sandstone, Wisconsin. *Clays and Clay Minerals*, **47**, 199–130.

Zwingmann, H. and Manckeltow, N. (2004) Timing of Alpine fault gouges. *Earth and Planetary Science Letters*, **223**, 415–425.

Zwingmann, H., Manckeltow, N., Antognini, M., and Lucchini, R. (2010a) Dating of shallow faults: New constraints from the AlpTransit tunnel site (Switzerland). *Geology*, **38**, 487–490.

Zwingmann, H., Yamada, K., and Tagami, T. (2010b) Timing of brittle deformation within the Nojima fault zone, Japan. *Chemical Geology*, **275**, 176–185.

(*Received 22 July 2015; revised 26 February 2016; Ms. 1020; AE: W.D. Huff*)